



Article

Remotely Sensing Phytoplankton Size Structure in the Mediterranean Sea: Insights from In Situ Data and Temperature-Corrected Abundance-Based Models

John A. Gittings ^{1,*}, Eleni Livanou ¹, Xuerong Sun ², Robert J. W. Brewin ², Stella Psarra ³, Manolis Mandalakis ⁴, Alexandra Peltekis ³, Annalisa Di Cicco ⁵, Vittorio E. Brando ⁵ and Dionysios E. Raitsos ¹

- Department of Biology, National and Kapodistrian University of Athens, 15772 Athens, Greece; eleniliva@biol.uoa.gr (E.L.); draitsos@biol.uoa.gr (D.E.R.)
- Centre for Geography and Environmental Science, Department of Earth and Environmental Sciences, Faculty of Environment, Science and Economy, University of Exeter, Cornwall TR10 9FE, UK; x.sun8@exeter.ac.uk (X.S.); r.brewin@exeter.ac.uk (R.J.W.B.)
- Institute of Oceanography, Hellenic Centre for Marine Research, 71003 Heraklion, Greece; spsarra@hcmr.gr (S.P.); a.pelteki@hcmr.gr (A.P.)
- Institute of Marine Biology, Biotechnology and Aquaculture, Hellenic Centre for Marine Research, 71003 Heraklion, Greece; mandalakis@hcmr.gr
- Consiglio Nazionale delle Ricerche, Istituto di Scienze Marine (CNR-ISMAR), 00133 Rome, Italy; annalisa.dicicco@artov.ismar.cnr.it (A.D.C.); vittorioernesto.brando@cnr.it (V.E.B.)
- * Correspondence: jagittings@biol.uoa.gr

Abstract

Since the mid-1980s, the Mediterranean Sea's surface and deeper layers have warmed at unprecedented rates, with recent projections identifying it as one of the regions most impacted by rising global temperatures. Metrics that characterize phytoplankton abundance, phenology and size structure are widely utilized as ecological indicators that enable a quantitative assessment of the status of marine ecosystems in response to environmental change. Here, using an extensive, updated in situ pigment dataset collated from numerous past research campaigns across the Mediterranean Sea, we re-parameterized an abundance-based phytoplankton size class model that infers Chl-a concentration in three phytoplankton size classes: pico- (<2 μm), nano- (2–20 μm) and micro-phytoplankton (>20 μm). Following recent advancements made within this category of size class models, we also incorporated information of sea surface temperature (SST) into the model parameterization. By tying model parameters to SST, the performance of the re-parameterized model was improved based on comparisons with concurrent, independent in situ measurements. Similarly, the application of the model to remotely sensed ocean color observations revealed strong agreement between satellite-derived estimates of phytoplankton size structure and in situ observations, with a performance comparable to the current regional operational datasets on size structure. The proposed conceptual regional model, parameterized with the most extended in situ pigment dataset available to date for the area, serves as a suitable foundation for long-term (1997-present) analyses on phytoplankton size structure and ecological indicators (i.e., phenology), ultimately linking higher trophic level responses to a changing Mediterranean Sea.

Keywords: phytoplankton size structure; ocean color; remote sensing; ecological indicators



Academic Editor: Raphael M. Kudela

Received: 29 April 2025 Revised: 20 June 2025 Accepted: 2 July 2025 Published: 9 July 2025

Citation: Gittings, J.A.; Livanou, E.; Sun, X.; Brewin, R.J.W.; Psarra, S.; Mandalakis, M.; Peltekis, A.; Di Cicco, A.; Brando, V.E.; Raitsos, D.E. Remotely Sensing Phytoplankton Size Structure in the Mediterranean Sea: Insights from In Situ Data and Temperature-Corrected Abundance-Based Models. *Remote Sens.* 2025, 17, 2362. https://doi.org/10.3390/rs17142362

Copyright: © 2025 by the authors. Licensee MDPI, Basel, Switzerland. This article is an open access article distributed under the terms and conditions of the Creative Commons Attribution (CC BY) license (https://creativecommons.org/licenses/by/4.0/).

Remote Sens. 2025, 17, 2362 2 of 31

1. Introduction

The Mediterranean Sea, often referred to as a "miniature ocean" [1], is arguably one of the most unique marine ecosystems on Earth. As the largest semi-enclosed sea (~2.5 million km²), the Mediterranean features a range of physical oceanographic processes (mesoscale gyres, sites of deep-water formation and thermohaline circulation) that shape its complex biophysical characteristics [2,3]. The basin's nutrient regimes range from oligotrophic to ultra-oligotrophic, with phosphorus being the predominant limiting nutrient, particularly in the Eastern Mediterranean Sea [4–7]. Nevertheless, the basin supports enhanced levels of phytoplankton biomass and primary production, particularly in regions characterized by cyclonic gyres, strong winter vertical mixing, fronts, coastal upwelling and inputs from anthropogenic sources [8–10]. Despite the general predominance of oligotrophy in the basin, such mechanisms contribute to increased biological productivity, which supports higher trophic levels and essential fisheries resources, as well as the Mediterranean Sea's status as a biodiversity hotspot [11–13].

Rising temperatures in Mediterranean surface and subsurface waters have been reported since the 1980s, and warming trends (~0.03–0.048 °C/year depending on the reference period and area of the basin) have continued into the present decade [3,14–19]. Furthermore, model-based analyses of the projected responses of the Mediterranean hydroclimate and regional atmospheric circulation have shown that the broader region is a hotspot for climate warming [20,21]. The reported impacts of increased temperatures on Mediterranean marine ecosystems include alterations to plankton community composition, abundance and phenology [22–25], harmful algal blooms [26] and jellyfish outbreaks [27]. Warmer conditions have also been linked with the entry of invasive tropical species [16,28–30] and changes to the biomass, distribution, spawning and landings of commercially important pelagic fish species [31–34]. A detailed review on the impacts of warming and temperature extremes on Mediterranean Sea marine ecosystems and biota is provided by Darmaraki et al. [35].

Ecological indicators based on the presence and distribution of phytoplankton, which constitute the base of marine food webs and contribute to approximately half of the annual global carbon fixation [36–38], can be used to quantify the health of marine ecosystems and their response to environmental perturbations and climate warming [39–41]. Remotely sensed observations of ocean color provide the only means from which long-term estimates of phytoplankton can be acquired synoptically at a high spatial resolution (<1 km) and sampling frequency (daily) [40]. A key ecological indicator for monitoring marine ecosystem health is phytoplankton size structure, which has important ramifications for biogeochemical cycling [42], the export of carbon to deeper layers [43–47] and marine food web structure [48–51].

Until now, there have been several concerted efforts dedicated to the satellite-based retrieval of size structure, and phytoplankton functional types (PFTs), in the Mediterranean Sea. Navarro et al. [52,53] used an updated version of the PHYSAT method [54,55], a spectral approach that analyzes normalized water-leaving radiances to reproduce and investigate the dynamics of four phytoplankton functional groups. Sammartino et al. [56] employed an abundance-based approach [57,58] to derive estimates of pico-, nano- and micro-phytoplankton from SeaWiFS observations of total chlorophyll-a (Chl-a) concentration and investigated their spatiotemporal variability. The authors based their abundance-based model re-parameterization on in situ pigment datasets acquired from two trans-Mediterranean oceanographic cruises (Prosope99 and Boum08) and the BOUSSOLE mooring situated in the Northwestern Mediterranean Sea. An alternative abundance-based model was later developed by Di Cicco et al. [59], who applied a statistical approach to the same in situ datasets to derive polynomial equations that describe the relationships

Remote Sens. 2025, 17, 2362 3 of 31

between total Chl-a concentration and three phytoplankton size classes, estimated through a regional Diagnostic Pigment Analysis/Approach (DPA). Their equations were subsequently applied to satellite-derived observations of the total Chl-a concentration to derive regional products of the phytoplankton size classes (PSCs) available in the European Union Copernicus Marine Service online catalog (https://doi.org/10.48670/moi-00299) [60,61]. Additional methods based on artificial intelligence clustering have also been utilized to study the spatiotemporal distribution of phytoplankton functional types from remotely sensed ocean color data [62].

Deriving phytoplankton size structure from satellite-derived observations of ocean color is not a trivial task [63]. The quality of the initial estimates of phytoplankton biomass (indexed by total Chl-a concentration [total Chl-a]) depends on several factors, including the choice of ocean color algorithm used to retrieve Chl-a, the Case-1 assumption that phytoplankton and other optically active substances (colored dissolved organic matter and non-algal particles) covary in a predictable manner [64] and the potentially shifting relationships between total Chl-a concentration and the physical environment, especially within the context of climate change [65–67]. Among the various methods for deducing PSCs from ocean color, abundance-based approaches relying on the observed relationships between total phytoplankton biomass and cell size are amongst the most readily applicable using principal observations of satellite-derived Chl-a concentration and have been shown to perform similarly with spectral- and ecological-based approaches [51,58,68].

Once parameterized, abundance-based PSC models simply require inputs of satellite-derived total Chl-a concentration, making them relatively simple to implement. These models can perform well across a range of oceanic environments [56,58,69–83]. The derived parameters of abundance-based models also offer meaningful and interpretable information about the regional environment. Additionally, the more recent incorporation of physical parameters, including sea surface temperature (SST) into abundance-based PSC models, has provided the foundation for accounting for the effects of temperature, either directly (metabolic responses) or indirectly (changes in nutrient availability through mixing) on phytoplankton communities. This integration also supports the subsequent improvement of ocean color models and their capacity to capture climate-driven changes in phytoplankton size structure [66,67,70,71,79]. Despite recent advancements in abundance-based PSC models and the incorporation of physical variables, there remains a need for updated, region-specific frameworks for the Mediterranean Sea that integrate new in situ data (especially in undersampled regions of the Eastern Mediterranean Sea) and refine the accuracy of satellite-derived estimates of phytoplankton size structure.

Here, we aim to improve the estimation of phytoplankton size structure in the Mediterranean Sea. Specifically, our objectives are to (1) utilize an updated in situ dataset of phytoplankton pigment concentrations compiled from various sampling initiatives across the Mediterranean Sea and to apply a DPA to retrieve in situ estimates of size-fractionated Chl-a concentration in three size classes: pico-, nano- and micro-phytoplankton; (2) use these in situ observations of phytoplankton size fractions to re-parameterize a conceptual, three-component abundance-based PSC model [58,71]; (3) incorporate an SST-dependency within the model framework that accounts for the impact of changes in the regional physical environment on the model parameters, considering recent advances in ocean color modeling and PSC algorithms [67]; and (4) apply the re-parameterized model to satellite-derived ocean color observations of Chl-a concentration and independently validate the remotely sensed estimates of phytoplankton size structure. Model performance is assessed relative to an SST-independent version of the model, as well as current operational datasets that have been developed for the Mediterranean Sea (https://doi.org/10.48670/moi-00299) [60,61].

Remote Sens. 2025, 17, 2362 4 of 31

Finally, we explore potential applications of the re-parameterized model and investigate long-term trends in the fraction of PSCs over the last ~27 years.

2. Materials and Methods

2.1. Materials

2.1.1. High-Performance Liquid Chromatography (HPLC) Pigment Datasets

HPLC pigment samples, collated from several databases, were acquired across the broader Mediterranean Sea. The SeaWiFS Bio-optical Archive and Storage System (SeaBASS) [84] offers HPLC pigment in situ datasets for different Mediterranean sampling campaigns, including the Prosope cruise (September–October 1999, https://campagnes. flotteoceanographique.fr/campagnes/99040060/, accessed on 1 December 2024) [85], the Boussole mooring (monthly sampling conducted between 2001 and 2006, as well as an independent sampling effort in July 2008) [86] and the Boum08 cruise (July 2008) [87]. A subset of pigment datasets was also acquired from the MAREDAT global database of HPLC phytoplankton pigment data measurements (https://doi.pangaea.de/10.1594/PANGAEA. 793246, accessed on 1 December 2024) [88]. The MAREDAT dataset comprises a collation of pigment data from different Mediterranean sampling campaigns, within the framework of broader European Programs. These campaigns include the ALMOFRONT1 cruise (Leg 2, May 1991, https://campagnes.flotteoceanographique.fr/campagnes/91004212/, accessed on 1 December 2024) and ALMOFRONT2 cruise (Leg 2, December 1997–January 1998, https://campagnes.flotteoceanographique.fr/campagnes/97010132/, accessed on 1 December 2024) [89,90], the MTPII-MATER/MINOS cruise (May-June 1996) [91], the METEOR 31/1 cruise (December 1994–February 1995) [92] and the DYFAMED cruises (January 1991–December 2005) [93]. Datasets were also acquired from the Tara Oceans (2009–2013) and Mediterranean (2014) expeditions (https://fondationtaraocean.org/en/ expedition/tara-oceans/, accessed on 1 December 2024). HPLC pigment measurements collected during the BioArgoMed oceanographic cruise (13 May 2015-1 June 2015) were also acquired from https://www.seanoe.org/data/00405/51678/ (accessed on 1 December 2024) [94].

In the Eastern Mediterranean Sea, the HPLC database maintained by the Hellenic Centre for Marine Research (HCMR) [95] consisted of observations collected during nine oceanographic cruises within the framework of European Union and national projects (SESAME-IP (2008), PERSEUS-IP (2013), KRIPIS I (October 2014, May and December–2015), LEVECO (2016) [96], JRC-SHIPSUPPORT I (2022) and the THALES-AegeanMarTech project (October 2013 and March and July 2014) [97]), as well as two time-series datasets collected from two monitoring stations of the POSEIDON system in the Cretan Sea; the E1-M3A buoy (WMO 61277), located 24 nautical miles north of Heraklion in Crete island (~35.736°N, 25.122°E), operating since 2010, and the Heraklion Coastal Buoy (HCB) at Heraklion Bay, Cretan Sea (35.425°N–25.073°), operating since 2016 [98,99].

Sampling stations often included multiple in situ measurements taken at various depths. For this analysis, we used pigment samples from the upper 20 m of the water column, which approximately corresponds to estimates of the first optical depth previously reported in the Mediterranean Sea [2,100]. Further justification for the selection of the upper 20 m is provided in Figure S1, which shows the ratio of total Chl-a in the surface layer to measurements at deeper depth intervals. Within the upper 20 m, this ratio remains relatively stable. However, at deeper intervals (>30 m), it becomes more variable, with differences in the surface-to-depth ratio reaching up to an order of magnitude. HPLC measurements were collated into a consolidated pigment dataset and subjected to the following quality assurance procedures. First, following Aiken et al. [101], samples were retained when (1) the difference between total Chl-a concentration and the sum of accessory

Remote Sens. 2025, 17, 2362 5 of 31

pigments was <30% of the total pigment concentration and (2) the regression between total Chl-a and the sum of accessory pigments exhibited a slope between 0.7 and 1.4 and an $r^2 > 0.9$. In addition, data points falling outside the 95% confidence interval of the regression were excluded. After applying these quality assurance procedures, a total of 2234 measurements were included in the analysis.

2.1.2. Auxiliary Size-Fractionated Chlorophyll-a and Phytoplankton Cell Abundance Datasets

The size-fractionated Chl-a dataset consists of in situ size-fractionated and fluorometrically assessed Chl-a data, concurrently collected with most of the HPLC-assessed pigment data in the database of HCMR. The size fractions employed were 0.2–2.0, 2.0–5.0 and >5.0 μ m. Further details for this dataset are provided in Psarra et al. [102]. Here, the 2.0–5.0 and >5.0 μ m fractions were combined, representing nano- and micro-phytoplankton. We note that Chl-a measurements within the picophytoplankton size class (0.2–2 μ m) were excluded when values were \leq 0.01 mg m⁻³ due to limitations in fluorometric detection at such low concentrations. Moreover, to obtain an estimation of the observed size ranges of the dinoflagellates in the Mediterranean Sea, a time-series dataset of larger nano- and microplankton cells (approximately >7 μ m cell size) collected at the E1-M3A station, spanning 12 years (2010–2022), was also analyzed. Phytoplankton species identification and counting were performed with inverted microscopy on 100 mL water subsamples preserved in alkaline Lugol's solution (final concentration 2%) [103].

Finally, to perform a preliminary assessment of the pigment composition per size fraction, a small-scale sampling scheme was designed. Briefly, sub-surface (~2 m) coastal seawater was collected from the north coast of Crete in front of HCMR facilities on 28 May 2022. The Cretan Sea is considered an oligotrophic area [104], and several mesocosm and microcosm experiments simulating oligotrophic conditions have been performed with water from this site [105–107]. Duplicate 1.5–2 L seawater samples were filtered sequentially through 5, 2 and 0.2 μm pore size polycarbonate filters, and HPLC pigment determination per size fraction was performed following the extraction and pigment quantification procedures used in HCMR's HPLC database [97]. To assess whether the use of polycarbonate filters versus GF/F filters had any effect on the obtained results of the size-fractionated HPLC dataset, two additional samples were taken: (1) a 2 L sample filtered through a 25 mm GF/F filter commonly employed in standard HPLC pigment analysis and (2) a 1 L sample filtered through a 47 mm \emptyset 0.2 μ m pore size polycarbonate filter. A small percent difference of +0.39% in total Chl-a was observed between the GF/F and polycarbonate filters. For all other pigments, the corresponding percentage differences varied between -23% and +24%.

2.1.3. Satellite Ocean Color Data and Data Partitioning for Model Training and Validation

For the computation of satellite matchups, 20-m depth-averaged in situ pigment samples were matched to satellite-derived estimates of total Chl-a concentration acquired from the Copernicus Marine Service Mediterranean Bio-Geo-Chemical, Level 3, daily Satellite Observations product (OCEANCOLOUR_MED_BGC_L3_MY_009_143) for the period spanning September 1997–July 2024 (Figure 1). Level 3, daily, mapped data of total Chl-a concentration, as well as current operational estimates of phytoplankton size structure (see Section 3.4), were acquired at a spatial resolution of 1 km from https://doi.org/10.48670/moi-00299 [59–61,108,109]. To increase the number of available satellite matchups, each pigment sample was matched to a 3×3 box of pixels, centered on the closest pixel to the in situ sampling station, based on the same day and nearest longitude and latitude [110]. Following previous homogeneity criteria for satellite ocean color matchup data, boxes containing less than 5 valid pixels and with a coefficient of variation > 0.15

Remote Sens. 2025, 17, 2362 6 of 31

were discarded [110,111]. For boxes containing more than 5 valid pixels, the median of the existing pixels was then computed. A total of 325 satellite matchups were retrieved based on the depth-averaged HPLC pigment dataset (Figure S3). For the partitioning of the HPLC in situ dataset (N = 2234) into subsets for model training and independent validation, we designated all sampling stations without a corresponding satellite observation as the training dataset (N = 1294). In situ samples that did have satellite matchups were set aside for independent validation (N = 940). We note that HPLC measurements at all available depths within the upper 20 m were incorporated in this partitioning.

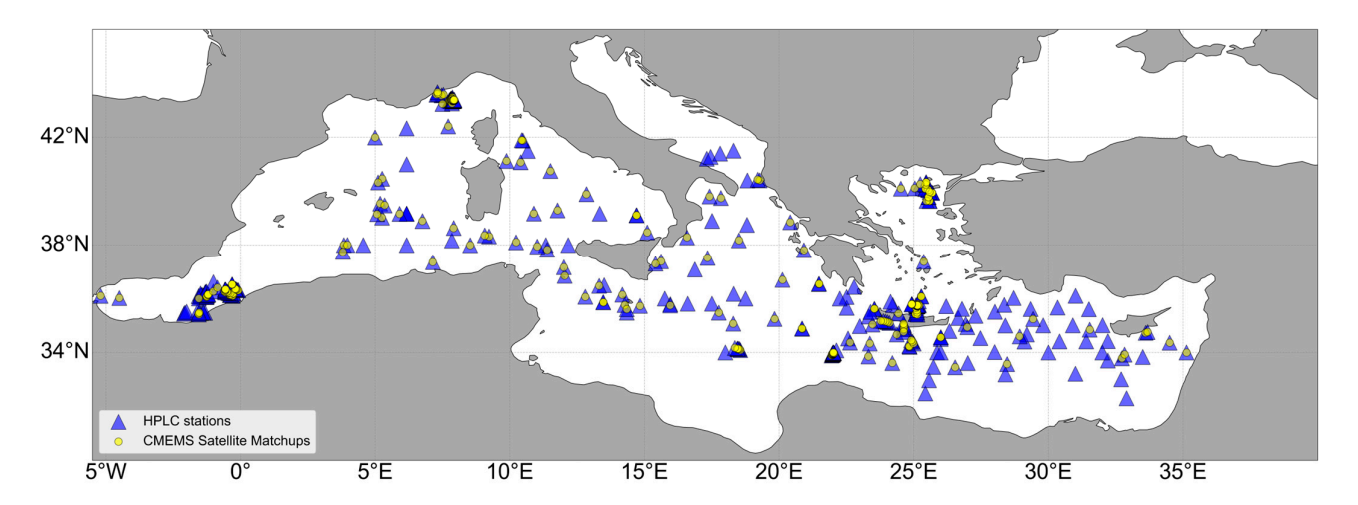


Figure 1. Spatial map highlighting the locations of the in situ pigment sampling stations in the Mediterranean Sea used for the model re-parameterization (blue triangles) and the corresponding satellite ocean color matchups used for model validation (yellow circles).

2.1.4. Satellite-Derived Sea Surface Temperature Datasets

Level 4 daily observations of SST were acquired at a spatial resolution of $0.05^{\circ} \times 0.05^{\circ}$ $(\sim 5.5 \times 5.5 \text{ km})$ from the Mediterranean Sea–High Resolution L4 Sea Surface Temperature Reprocessed Product, located in the Copernicus Marine Data Stores (https://data.marine. copernicus.eu/product/SST_MED_SST_L4_REP_OBSERVATIONS_010_021/description, https://doi.org/10.48670/moi-00173 [112], accessed on 1 February 2025). This reprocessed dataset, produced specifically for the Mediterranean Sea, provides a long-term, continuous SST time series, consisting of nighttime, optimally interpolated satellite-derived observations spanning from January 1982 to present day. SST matchups were acquired by retrieving the closest satellite pixel to the in situ training sample based on the nearest longitude and latitude for the same day. We note that this dataset has been validated with an extensive in situ temperature dataset in a coastal region of the Mediterranean Sea (Saronikos Gulf, Aegean Sea). Comparisons between in situ data and the satellite-derived SST product have revealed strong and highly significant correlations (r > 0.99, p < 0.00001) [10]. For the SST-dependent model applications involving remotely sensed total chlorophyll-a (Chl-a) estimates and the computation of annual trends (Section 3.5), monthly SST fields were interpolated (griddata function from the SciPy library in Python) to match the spatial resolution of the ocean color dataset (OCEANCOLOUR_MED_BGC_L3_MY_009_143).

2.2. Methods

2.2.1. Diagnostic Pigment Approach

To compute phytoplankton size fractions from HPLC pigment datasets, we adopted the method of Brewin et al. [70], modified from Claustre [113], Vidussi et al. [92], Uitz et al. [114], Brewin et al. [58], Devred et al. [115] and Di Cicco et al. [59]. First, the total Chl-a

Remote Sens. 2025, 17, 2362 7 of 31

concentration (C) was computed from the weighted sum of seven diagnostic phytoplankton pigments (henceforth referred to as C_w), according to

$$C_w = \sum_{i=1}^7 W_i P_i \tag{1}$$

where W represents the weights, and P corresponds to the following seven diagnostic pigments, numbered sequentially as follows: (1) fucoxanthin, (2) peridinin, (3) 19'-hexanoyloxyfucoxanthin, (4) 19'-butanoyloxyfucoxanthin, (5) alloxanthin, (6) total chlorophyll-b and (7) zeaxanthin. Following this, W was calculated by applying a multi-linear least squares regression to the pigment samples. The statistical performance regarding the relationship between C_w and the measured concentration of total Chl-a concentration (C), as well as a comparison of W values relative to the previous literature, are presented in Figure S2 and Table S1, respectively.

Next, we computed the fraction of total Chl-a concentration within three PSCs: pico-, nano- and micro-phytoplankton. Following Brewin et al. [58], and as applied by Di Cicco et al. [59] to in situ pigment datasets mainly from the Western Mediterranean Sea, the fraction of pico-phytoplankton (F_p , cell diameter < 2.0 μ m) was computed by assigning zeaxanthin, total chlorophyll-b and a portion of 19'-hexanoyloxyfucoxanthin to the pico-phytoplankton assemblage at total Chl-a concentrations < 0.08 mg m⁻³:

$$F_p = \begin{cases} \frac{(-12.5C+1)W_3P_3}{C_w} + \frac{\sum_{i=6}^{7} W_i P_i}{C_w} & \text{if } C \leq 0.08 \text{ mg m}^{-3} \\ \frac{\sum_{i=6}^{7} W_i P_i}{C_w} & \text{if } C > 0.08 \text{ mg m}^{-3} \end{cases}$$
(2)

The fraction of the total Chl-a concentration of the nano-phytoplankton assemblage (F_n) was determined by assigning 19-butanoyloxyfucoxanthin, alloxanthin and the remaining portion of 19'-hexanoyloxyfucoxanthin following

$$F_n = \begin{cases} \frac{(12.5C)W_3P_3}{C_w} + \frac{\sum_{i=4}^5 W_i P_i}{C_w} & \text{if } C \leq 0.08 \text{ mg m}^{-3} \\ \frac{\sum_{i=3}^5 W_i P_i}{C_w} & \text{if } C > 0.08 \text{ mg m}^{-3} \end{cases}$$
(3)

Finally, the fraction of total Chl-a concentration to the micro-phytoplankton assemblage (F_m) was computed by assigning fucoxanthin and peridinin, following

$$F_m = \left\{ \begin{array}{l} \frac{\sum_{i=1}^{2} W_i P_i}{C_{m}} \end{array} \right. \tag{4}$$

After deriving the fractions of each phytoplankton assemblage to total Chl-a concentration (F_p , F_n and F_m), the size-specific Chl-a concentrations for each size class were computed by multiplying each size fraction by the measured total Chl-a concentration as follows:

$$C_p = F_p C (5)$$

$$C_n = F_n C (6)$$

and

$$C_m = F_m C \tag{7}$$

2.2.2. SST-Independent Three-Component Phytoplankton Size Class Model

We applied the three-component abundance-based model of Brewin et al. [58], which estimates the fractional contribution of different PSCs as a continuous function of the total Chl-a concentration (ranging from 0.006 to 5.512 mg m⁻³ in this study). Based on previous research by Sathyendranath et al. [116], the empirical model assumes that the dominance of small phytoplankton cells (picophytoplankton) occurs up to a specific total

Remote Sens. 2025, 17, 2362 8 of 31

Chl-a concentration. Beyond this upper limit of total Chl-a, regulated by a combination of bottom up (e.g., nutrient availability) and top down (e.g., grazing), the addition of extra Chl-a into the marine ecosystem can be attributed to the growth of larger phytoplankton cells (nano- and micro-phytoplankton) [42,51,117]. These relationships can be represented mathematically using the two following exponential functions that relate the total Chl-a concentration (C) to the fractional contribution of Chl-a in the picophytoplankton (F_p) and combined pico-/nanophytoplankton ($F_{p,n}$) assemblages (Equations (8) and (9)):

$$F_p = \frac{C_p^m \left[1 - exp\left(-\frac{D_p}{C_p^m} C \right) \right]}{C} \tag{8}$$

$$F_{p,n} = \frac{C_{p,n}^m \left[1 - exp\left(-\frac{D_{p,n}}{C_{p,n}^m}C \right) \right]}{C} \tag{9}$$

In Equations (8) and (9), the model parameters C_p^m and $C_{p,n}^m$ represent the asymptotic maximum Chl-a concentrations attainable by the picophytoplankton and combined pico-/nanophytoplankton assemblages, whilst D_p and $D_{p,n}$ characterize the fraction of total Chl-a for each assemblage as total Chl-a tends to zero. The model parameters were derived by fitting Equation (8) to F_p and C, and Equation (9) to $F_{p,n}$ and C, which were computed using the in situ HPLC dataset (see Section 2.2.1 and Equations (2)–(4)). To apply the fits, we used a non-linear least squares fitting procedure ("leastsq: Levenberg-Marquardt" method from the *lmfit* package in Python [version 1.2.2]). As size-fractionated Chl-a within the modeled PSCs (F_p and $F_{p,n}$) cannot exceed the total Chl-a concentration, the parameters D_p and $C_{p,n}^m$ were constrained to be less than or equal to 1. The parameters C_p^m and $C_{p,n}^m$ were constrained to be less than or equal to 5.51 mg m⁻³. This upper bound was arbitrarily chosen to reflect a realistic theoretical maximum concentration of total Chl-a in the study region. To compute the uncertainties of the model parameters, we implemented a bootstrapping procedure [118] by randomly sub-sampling the training dataset (1000 iterations) and re-fitting Equations (8) and (9) to each sub-sample. The median and 95% confidence intervals were then retrieved from the resultant parameter distribution. The computed model parameters are presented in Table 1 and generally lie within the range of values previously retrieved in other areas of the global oceans. The fractional contributions of the nanophytoplankton and microphytoplankton assemblages were subsequently derived as follows:

$$F_n = F_{p,n} - F_p \tag{10}$$

$$F_m = 1 - F_{p,n} \tag{11}$$

The corresponding Chl-a concentration associated with each size class can be derived by multiplying F_p , F_n and F_m by the total Chl-a concentration.

Table 1. Parameters of the SST-independent and SST-dependent models and comparisons with parameters computed in previous studies. The bracketed values represented the 95% confidence intervals computed using bootstrapping (3000 iterations).

Model			SST- Independent Model						SST-Dependent Model		
Study	This study	[58]	[119]	[70]	[71]	[73]	[67]		This study	[71]	[67]
Region	Mediterranean Sea	Atlantic Ocean	Indian Ocean	Global	North Atlantic Ocean	Northeast Atlantic Ocean	Global		Mediterranean Sea	North Atlantic Ocean	Global
N	1294	1935	686	5841	2239	1100	30,579				
$C_{p,n}^{m}$ (mg m ⁻³)	2.15 (1.71–2.63)	1.06	0.94	0.77 (0.72–0.84)	0.82 (0.76–0.88)	0.28	0.95 (0.927-0.968)				
								G1	-1.57 $(-2.181.45)$	-1.51 (-1.571.43)	-0.56 $(-0.5620.549)$
								G2	-3.51 (-4.212.45)	-1.25 (-1.411.25)	-3.79 (-4.0533.549)
								G3	12.83 (12.59–12.87)	14.95 (14.87–15.05)	1.92 (1.888–1.944)
								G4	-0.14 $(-0.160.11)$	0.25 (0.23–0.26)	-0.14 $(-0.1420.137)$
$C_p^m (\text{mg m}^{-3})$	0.10 (0.09–0.12)	0.11	0.17	0.13 (0.12-0.14)	0.13 (0.12-0.13)	0.06	0.17 (0.167–0.174)				
								H1	0.24 (0.16-0.26)	0.29 (0.28-0.30)	-0.28 (-0.2790.272)
								H2	0.58 (0.47-0.77)	3.05 (2.87–3.26)	1.13 (1.070–1.187)
								Н3	12.00 (12.00–12.90)	16.24 (16.19–16.29)	5.03 (4.957–5.103)
								H4	0.69 (0.68–0.75)	0.56 (0.55-0.57)	0.89 (0.892–0.898)
$D_{p,n}$	0.87 (0.86–0.88)	0.9	0.97	0.94 (0.93-0.95)	0.87 (0.86-0.89)	0.96	0.87 (0.868-0.878)				
								J1	0.048 (0.046–0.070)	0.37 (0.367–0.373)	0.39 (0.390-0.392)
								J2	5.20 (-14.41-5.76)	1.13 (1.10–1.16)	0.33 (0.330-0.333)
								J3	12.91 (12.89–17.99)	14.89 (14.87–14.91)	8.02 (8.000-8.047)
								J4	0.853 (0.821–0.854)	0.569 (0.566–0.571)	0.55 (0.546-0.547)
D_p	0.60 (0.56–0.64)	0.73	0.82	0.80 (0.78-0.82)	0.73 (0.71–0.76)	0.99	0.67 (0.658–0.675)				
	(0.00 0.0-)							<i>O</i> 1	0.66 (0.52-1.10)	0.503 (0.501–0.505)	0.65 (0.647-0.650)
								O2	0.35 (-2.30-0.49)	1.33 (1.31–1.37)	0.22 (0.222-0.224)
								O3	12.00 (12.00–12.54)	17.31 (17.28–17.32)	12.79 (12.772–12.800)
								<i>O</i> 4	0.09 (0–0.52)	0.258 (0.256–0.259)	0.09 (0.085–0.087)

2.2.3. SST-Dependent Three-Component Phytoplankton Size Class Model

Here, we examine how SST influences the relationship between total chlorophyll-a concentration and phytoplankton size structure. Specifically, we relate the parameters of the model to SST based on the framework proposed by Brewin et al. [71] and Sun et al. [67]. The training dataset was sorted according to increasing SST, and a running fit of the model was performed using a range of bin sizes ranging from 550 to 950 samples at increments of 20. Equations (8) and (9) were applied to the data within each bin, which was incrementally shifted by one sample from lower to higher temperatures. A bootstrap approach with 1000 iterations was used to estimate the model parameters for each running fit, with the median of the bootstrap distribution taken as the final parameter value. The results, including the variation in model parameters with rising temperatures across all bin sizes, are presented in Figure 2. To represent the relationships between SST and the model parameters, we applied the following logistic functions to the running model fits using a non-linear least squares minimization approach ("leastsq: Levenberg-Marquardt" method from the *lmfit* package in Python), following Brewin et al. [71] and Sun et al. [67]:

$$C_{p,n}^{m} = 1 - \left\{ \frac{G_a}{1 + exp[-G_b(SST - G_c)]} + G_d \right\}$$
 (12)

$$C_p^m = 1 - \left\{ \frac{H_a}{1 + exp[-H_b(SST - H_c)]} + H_d \right\}$$
 (13)

$$D_{p,n} = \frac{J_a}{1 + exp[-J_b(SST - J_c)]} + J_d$$
 (14)

$$D_p = \frac{O_a}{1 + exp[-O_b(SST - O_c)]} + O_d$$
 (15)

Here, the model parameters G_a and G_d represent the upper and lower bounds of $C_{p,n}^m$, G_b denotes the slope of the change in $C_{p,n}^m$ with SST and G_c represents the mid-point of the slope between $C_{p,n}^m$ and SST. For the model parameters C_p^m , $D_{p,n}$ and D_p , H_i , J_i and O_i (i = a - d) are broadly equivalent to G_i in Equation (12). The values of the model parameters, as well as their associated 95% confidence intervals, are presented in Table 1.

Overall, the relationships between the model parameters and SST are comparable to what has been reported in other regions [67,71], including the adjacent oligotrophic Red Sea [66], where $C_{p,n}^m$ and C_p^m decrease with rising SSTs (Figure 2a,c), and $D_{p,n}$ and D_p increase. Using smaller bin sizes (e.g., <670 data points), there are insufficient data across the full range of Chl-a to reliably retrieve model parameters. In these cases, the running fit may include subsets of data lacking sufficient sample size or variability, often resulting in the parameter $C_{p,n}^m$ reaching its upper bound (~5.51 mg m⁻³) (Figure 2c). Conversely, using larger bin sizes likely provides a bin of data points that is more representative of the overall dataset, allowing the model to be better constrained and to more effectively capture relationships in the dataset. To illustrate this more clearly, we present fits of the three-component model for the retrieval of $C_{p,n}$, using smaller (550 samples) and larger (910 samples) bin sizes. These fits are applied to the section of the sorted training dataset where the model parameter $C_{p,n}^m$ upper bound is reached, providing a comparative view of how bin size influences the model's behavior (Figure S4). Using a larger bin size, the improved ability to retrieve the model parameter $C_{p,n}^m$ is visually apparent, enabling a more realistic estimation of size-specific Chl-a concentration for the pico-/nano-phytoplankton size class (Figure S4).

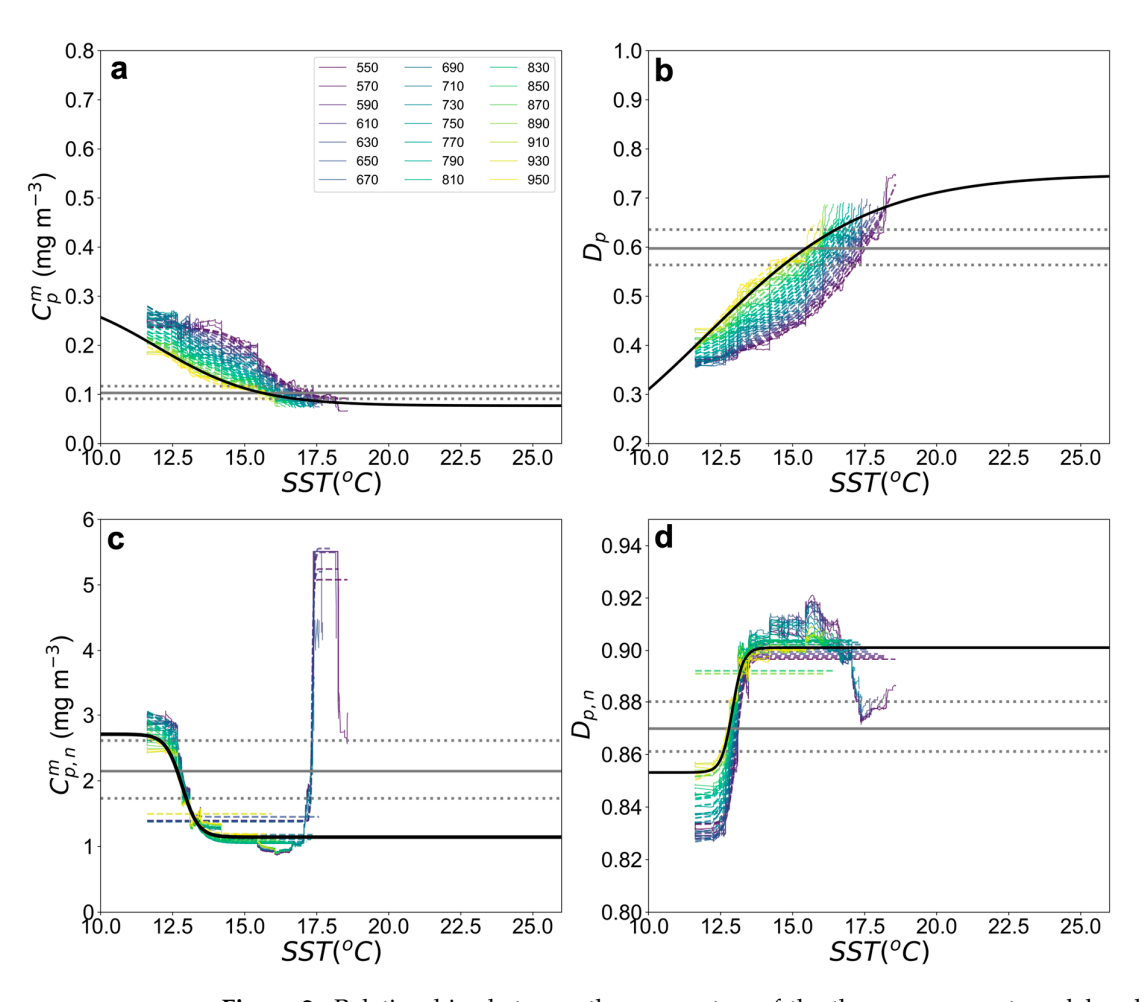


Figure 2. Relationships between the parameters of the three-component model and sea surface temperature. (**a,b**) Variations in the model parameters C_p^m and D_p as a function of temperature. The solid-colored lines represent the running fits of the model for different bin sizes (550–950 samples). The corresponding dashed-colored lines represent the logistic functions used to characterize the relationships between C_p^m and D_p and temperature (Equations (13) and (15)). Depending on the bin size, some notable difference can be observed in the fitted models, particularly at smaller bin sizes. The solid black lines highlight the result of the least squares minimization using a bin size of 910 samples. The gray solid and dotted lines represent the parameters of the SST-independent model and their uncertainties, respectively (**c,d**), as shown in panels (**a,b**) but for $C_{p,n}^m$ and $D_{p,n}$ (Equations (12) and (14)).

For the implementation of the temperature dependency, we subsequently chose a larger bin size of 910 samples as this yielded improved statistical performance metrics on the residuals of the fitted logistic model and produced optimal results in the in situ validation (see Section 3.3).

2.2.4. Statistical Performance Metrics

For the assessment of satellite ocean color data and the in situ validation of the reparameterized PSC model, we used a suite of statistical performance metrics, including the Pearson correlation coefficient (r), the Root Mean Square Error (Ψ), the Mean Absolute Error (ϵ) and the systematic bias (δ). These metrics have been used previously in satellite ocean color studies for the purpose of model validation [66,67,69–72,79,81] and comprise key metrics prioritized by the European Space Agency Ocean Colour Climate Change

Remote Sens. 2025, 17, 2362 12 of 31

Initiative (ESA OC-CCI) project for the provision of per-pixel errors in satellite ocean color datasets [111]. The statistical error metrics and bias were computed as follows:

$$r = \sum \left(X_i^E - \overline{X}^E \right) \left(X_i^M - \overline{X}^M \right) / \sqrt{\left[\sum \left(X_i^E - \overline{X}^E \right)^2 \times \sum \left(X_i^M - \overline{X}^M \right)^2 \right]}$$
(16)

$$\varepsilon = \frac{\sum_{i=1}^{N} \left| X_i^E - X_i^M \right|}{N} \tag{17}$$

$$\psi = \left[\frac{1}{N} \sum_{i=1}^{N} \left(X_i^E - X_i^M \right)^2 \right]^{1/2} \tag{18}$$

$$\delta = \frac{1}{N} \left[\sum_{i=1}^{N} \left(X_i^E - X_i^M \right) \right] \tag{19}$$

where X is the variable (e.g., Chl-a concentration or fraction), the superscripts E and M represent estimated and measured variables, respectively, and N is the number of samples. In Equation (16), \overline{X}^E and \overline{X}^M represent the mean of the expected and measured variables respectively. Condorcet's pairwise comparisons of residuals was performed as an additional test of model performance [120–123] (see Supplementary Materials).

3. Results and Discussion

3.1. Three-Component Model Re-Parameterization

First, we fitted the re-parameterized SST-independent three-component PSC model to the training dataset (solid black lines in Figure 3). Overall, the model effectively captures the relationships between the total Chl-a concentration and the phytoplankton size fractions $(F_p, F_n, F_{p,n} \text{ and } F_m)$ (Figure 3a–d). F_p is higher at low total Chl-a concentrations, whilst F_n and F_m are greatest at intermediate and higher total Chl-a concentrations, respectively. These relationships are consistent with other applications of this model framework in other regions of the global oceans [58,69–72,74–76,79–81,124]. F_p dominates total phytoplankton biomass at Chl-a concentrations below ~0.1 mg $\rm m^{-3}.\ Between\ \sim\!0.1\ mg\ m^{-3}$ and ~3 mg m⁻³, F_n contributes the largest fraction. At concentrations exceeding ~3 mg m⁻³, F_m becomes the dominant size class. Whilst the upper boundary of total Chl-a associated with F_v (~0.1 mg m⁻³) is close to that reported in previous studies (~0.2 mg m⁻³) [58,73], the increase in microphytoplankton occurs at substantially higher total Chl-a concentrations, likely reflecting the general dominance of pico- and nanophytoplankton across a broader range of total Chl-a concentrations in the oligotrophic waters of the Mediterranean Sea [8,53,56,59,92,125–129]. The dominance of microphytoplankton at substantially higher Chl-a concentrations is likely linked to ephemeral events that substantially enhance nutrient availability, such as intense vertical winter mixing, upwelling, fronts, deep water formation, aeolian inputs from atmospheric deposition and anthropogenic inputs from coastal areas [8,56,125,126,130], which may enable the proliferation of larger phytoplankton groups such as diatoms.

The three-component model also successfully captures the relationship between total Chl-a concentration and size-specific Chl-a concentrations (C_p , C_n , $C_{p,n}$ and C_m) (Figure 3e–h). Following the assumptions of the conceptual three-component size class model, the static asymptotic maximum Chl-a concentrations theoretically attained by the picophytoplankton (C_p^m) and combined pico/nano-phytoplankton ($C_{p,n}^m$) assemblages (Equations (8) and (9)) can be visualized by the plateaus of the fitted models in Figure 3e,g. These asymptotic maximum values increase with phytoplankton size, where $C_p^m = 0.10 \text{ mg m}^{-3}$ and $C_{p,n}^m = 2.15 \text{ mg m}^{-3}$ (Table 1). The model underestimates F_p and overestimates F_n at lower total Chl-a concentrations (Figure 3a,b). This can also be observed when the model is fitted to the size-specific Chl-a concentrations (C_p and C_n) (Figure 3e,f).

This may be attributed to the influence of temperature on the relationships between total Chl-a concentration and phytoplankton size, where higher SSTs are associated with increased F_p and decreased F_n and F_m . The apparent temperature-dependency of the model parameters aligns with previous applications of the three-component model [67,71,79]. We also acknowledge that the initial assignment of pigments in the diagnostic pigment analysis (DPA) used to generate the training dataset could influence model performance as certain pigments—such as 19'-hexanoyloxyfucoxanthin—are shared by both pico- and nanophytoplankton groups. Consequently, the under- or over-representation of these groups in the model output may reflect biases introduced by pigment assignment. We refer the reader to Section 3.6 for further discussion on the modification of the DPA.

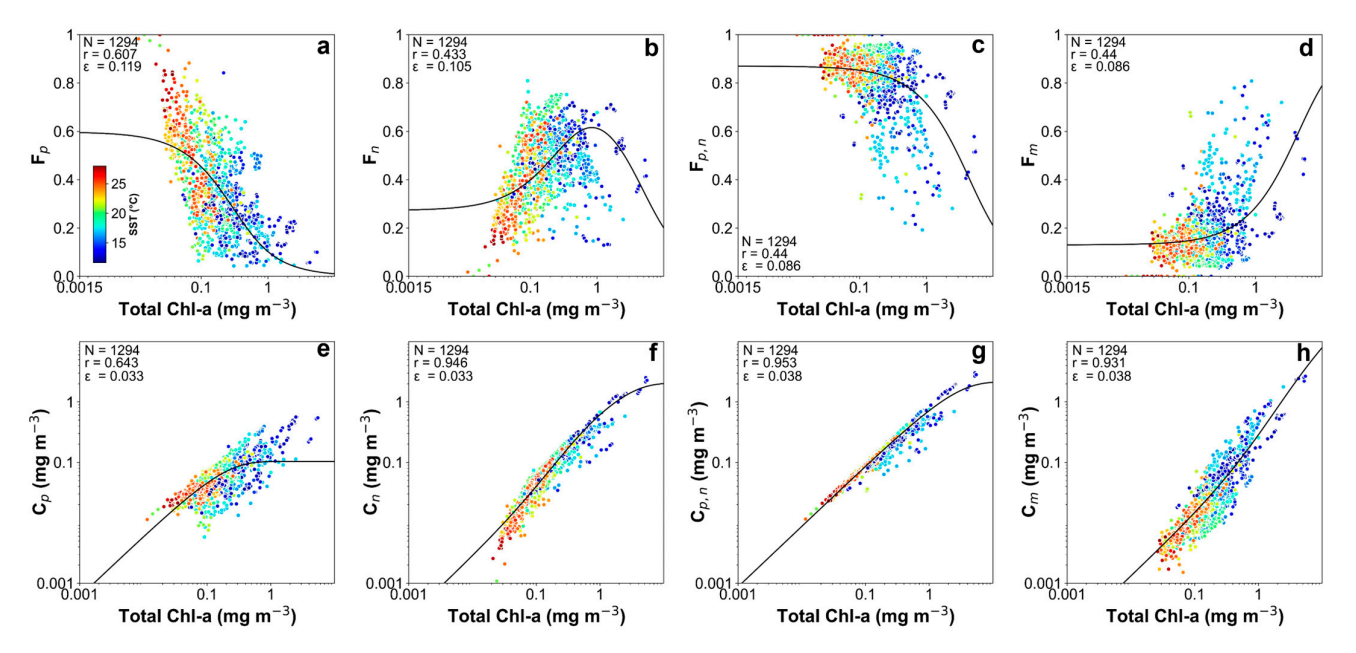


Figure 3. (a–d) Fits of the re-parameterized three-component model to the HPLC training dataset. The fraction of total Chl-a, partitioned into the phytoplankton size classes (F_p , F_n , $F_{p,n}$ and F_m), plotted as a function of total Chl-a concentration. The in situ data points have been plotted according to their corresponding sea surface temperature. The black solid line represents the fit of the three-component phytoplankton size class model (e–h). The corresponding size-specific Chl-a concentrations (C_p , C_n , $C_{p,n}$ and C_m), plotted as a function of total Chl-a concentration.

3.2. Incorporation of Temperature Dependency into the Three-Component Model

To investigate the impacts of temperature on the relationships between phytoplankton size structure and total phytoplankton biomass, we modified the abundance-based model following the approach of Brewin et al. [71] and Sun et al. [67] and incorporated a temperature-dependency within the conceptual model framework (see Section 2.2.3 in Materials and Methods). The resultant, simulated relationships between phytoplankton size fractions and size-specific Chl-a concentrations, incorporating the SST-dependent reparameterization, are presented in Figure 4. SST clearly influences the derived model fits for all PSCs; under warmer conditions, F_p increases at lower total Chl-a concentrations, while these conditions are associated with reductions in F_n and F_m at similarly low total Chl-a levels (Figure 4a-d). Conversely, colder temperatures are generally linked with a higher contribution of F_n and F_m , although some lower values of F_m do occur at higher Chl-a concentrations (>1 mg m⁻³), relative to $F_{p,n}$. Whilst these relationships are generally consistent across the full range of Chl-a concentrations, some exceptions do occur. For example, at intermediate total Chl-a concentrations (\sim 0.3–1 mg m⁻³), the contribution of F_p under warmer conditions decreases, coinciding with an increased contribution of F_n (Figure 4b). When considering F_m , the temperature-dependency effect is less apparent,

with relatively minor differences occurring in the estimated fraction across the full range of total Chl-a concentration (Figure 4d).

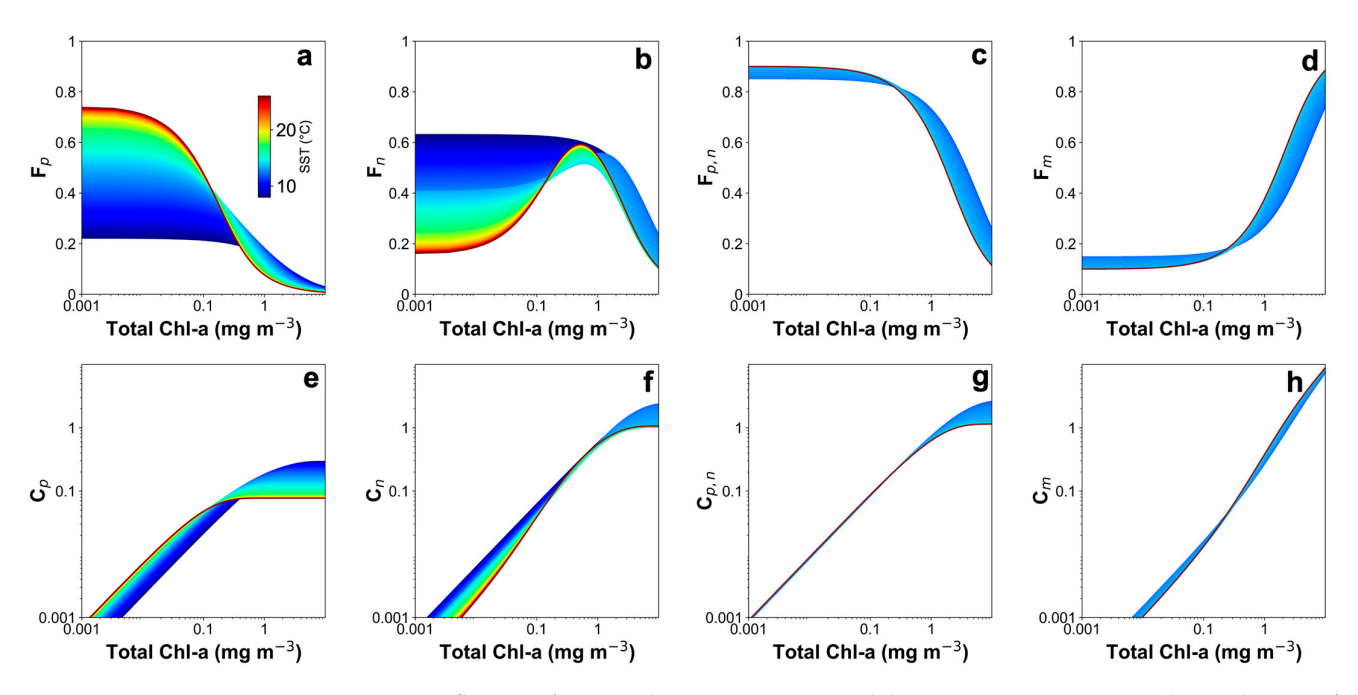


Figure 4. Influence of SST on three-component model re-parameterization. (**a**–**d**) Simulations of the fraction of total Chl-a, partitioned into the independent phytoplankton size classes (F_p , F_n , $F_{p,n}$ and F_m), plotted as a function of total Chl-a concentration for varying SSTs. (**e**–**h**) As shown in panels (**a**–**d**) but for the corresponding size-specific Chl-a concentrations (C_p , C_n , $C_{p,n}$ and C_m).

Overall, these relationships are consistent with previous studies [66,71,83,124] and may reflect the established linkages between phytoplankton size structure and the regional physical conditions. For example, the contribution of picophytoplankton to total biomass has been shown to be higher during warmer conditions in the oligotrophic waters of the Mediterranean Sea [22,131–135], reflecting the improved ability of smaller phytoplankton cells to flourish in more stratified, nutrient-depleted conditions [42,136–140]. Conversely, colder temperatures often indicate enhanced nutrient availability due to water column vertical mixing and deep convection events, which tend to favor blooms of larger phytoplankton cells [62,102,124,125,130,138,141]. In the Mediterranean Sea, bloom events may consist of both nanophytoplankton (e.g., nanoeukaryotes, nanoflagellates and nanoplanktonic diatoms) [53,130,142] and microphytoplankton (diatoms) [56,59,102,143], potentially explaining why, under colder temperatures, F_n remains higher than F_m as total Chl-a increases to intermediate concentrations (up to 1 mg m⁻³) (Figure 4d). Elevated concentrations of microphytoplankton have also been reported in Mediterranean coastal regions due to enhanced nutrient input from terrestrial sources [53,56,59,144], indicating potential exceptions to these relationships. Size-fractionated Chl-a concentrations, modeled as a function of SST (Figure 4e–h), exhibit similar relationships, with higher C_p values co-occurring with warmer temperatures up to intermediate concentrations of total Chl-a, beyond which C_n increases (Figure 4e,f).

3.3. Independent Model Validation

The independent model validation in situ dataset (N = 940, see Section 2.1.3) was used to compare the performance of the re-parameterized SST-independent model and SST-dependent models (Figure 5). Overall, the SST-independent model performs well for the retrieval of size-fractionated Chl-a concentrations (C_p , C_n , $C_{p,n}$ and C_m), with statistical

performance metrics ranging as follows: r = 0.76–0.99, Ψ = 0.05–0.26, ε = 0.04–0.21 and δ = -0.01–0.11 (Figure 5a–d).

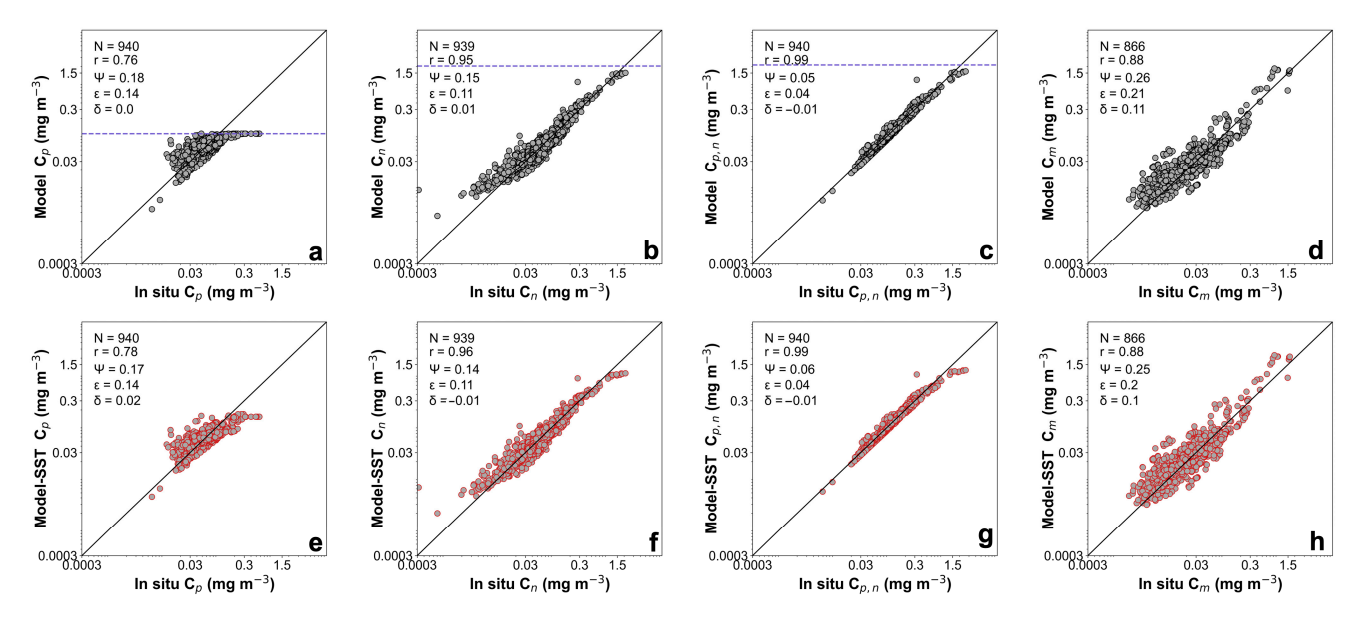


Figure 5. Independent PSC model validation between in situ and modeled size-fractionated Chl-a concentrations in the Mediterranean Sea. (\mathbf{a} – \mathbf{d}) Comparison of in situ size-fractionated Chl-a concentrations (C_p , C_n , $C_{p,n}$ and C_m) with modeled values using the SST-independent three-component model. The dashed purple lines represent the asymptotic maximum values of Chl-a concentration within each size class (see Equations (8) and (9)). The 1:1 line is shown as the solid black line. (\mathbf{e} – \mathbf{h}) As shown in panels (\mathbf{a} – \mathbf{d}) but incorporating the SST-dependency described in Section 2.2.3. Note that the difference in the number of observations between the nano- (N = 939) and microphytoplankton (N = 866) size classes is due to the dominance of picophytoplankton or the combined presence of pico- and nano-phytoplankton in those samples.

The SST-dependent model is not constrained by static asymptotic maximum values (C_p^m) and $C_{p,n}^m$, red dashed lines in Figure 5a-c) and performs equally well, or better, than the SST-independent model (Figure 5e-h). Specifically, there is an improvement in the correlation coefficient and error metrics of C_v (r = 0.78, Ψ = 0.17, ε = 0.14 verses r = 0.76, $\Psi = 0.18$ and $\varepsilon = 0.14$), particularly within the higher range of concentrations. The SST-dependent model performance for C_n and C_m is similar to that of the SST-independent model (Figure 5f,h). The improvement of C_p from the SST-dependent model is consistent with prior studies [67,71,79,83,145], reflecting its improved ability to capture C_v at higher concentrations. This may be attributed to the ability of the SST-dependent model to better capture the ecological relationships between size structure and total Chl-a, which may become more complex at higher concentrations. For example, the SST-model dependency potentially allows a better differentiation between intermediate or higher Chl-a regimes driven by vertical mixing of colder, nutrient-rich waters (favoring larger cells) and higher Chl-a regimes that occur in warmer, stratified conditions (favoring pico-phytoplankton). We also compared in situ and modeled estimates of size-fractionated Chl-a concentrations based on the full training dataset used to re-parameterize the model (N = 1294, Figure S5). The results of this comparison are consistent with the independent model validation presented in Figure 5; there is a substantially improved statistical performance for the retrieval of C_v , especially at higher concentrations, whilst the model performance for C_n , $C_{p,n}$ and C_m remains similar or slightly improved (Figure S5).

3.4. Satellite Validation

Based on the reasonable performance of the conceptual three-component model when validated against an independent in situ dataset (Figure 5), we applied this model, along with its SST-dependent counterpart, to satellite-derived matchups of Chl-a concentration. We then compared the results with corresponding in situ size-fractionated Chl-a concentrations (Figure 6). In addition, we compared the performance of the two re-parameterized three-component models presented here (SST-independent and SST-dependent) with the current operational Mediterranean dataset, which provides daily satellite-derived estimates of phytoplankton size structure from the Copernicus Marine Datastore (OCEANCOLOUR_MED_BGC_L3_NRT_009_141, Italian National Research Council, https://doi.org/10.48670/moi-00299 [59-61]) (Figure 6a-d) across the Mediterranean Sea. Performing the validation of the three aforementioned models based on the satellite derived Chl-a concentration is deemed appropriate considering the significant, positive correlation between HPLC-derived measurements of total Chl-a concentration and the satellite matchups reported here ($\mathbf{r} = 0.83$, $\mathbf{\Psi} = 0.25$, $\boldsymbol{\varepsilon} = 0.21$ and $\boldsymbol{\delta} = -0.14$, Figure S3), as well as the recent total Chl-a matchup analysis presented in Collela et al. [61].

To ensure complete independence of the satellite validation and maintain comparability among the different PSC models, we excluded all in situ datasets that were used during the development of the operational Copernicus product (Di Cicco et al. [59]), leaving 172 available satellite matchup data points. Generally, across the three different models, satellite-derived estimates of size-fractionated Chl-a concentration agree well with the independent in situ validation dataset (Figure 6). The SST-independent model (Figure 6e-h) performs similarly or slightly poorer than the current Copernicus operational product (Figure 6a-d). The main improvement of the SST-independent model can be observed in the error metrics for the retrieval of C_n (Figure 6f), with slight improvements in Ψ , ε and δ . When considering the SST-dependent model (Figure 6i–l), some improvements occur when compared to the Copernicus operational product and the SST-independent model. The correlation coefficient between in situ and satellite-derived estimates of C_p is improved (r = 0.71), coinciding with comparable model errors ($\Psi = 0.19$, and $\varepsilon = 0.14$), although δ from the Copernicus operational product remains lower ($\delta = -0.01$) in comparison to the SST-dependent model ($\delta = -0.04$). Additional improvements can be observed for the retrieval of satellite-derived estimates of C_n and C_m , which also exhibit comparable correlation coefficients and reductions in their respective model errors and biases (Figure 6j,l). The performance of the three models can be further visualized and compared in Figure S6, which also incorporates the results of the Condorcet's pairwise comparisons of the residuals test. Whilst the model errors are comparable, C_p and $C_{p,n}$ derived from the Copernicus operational product demonstrate a higher percentage of wins and improved bias compared to both the SST-independent and SST-dependent models. In contrast, C_n and C_m show comparable or higher win percentages, alongside the general improvement in error metrics, for the SST-independent and SST-dependent models. Collectively, these results demonstrate that both empirical [59–61] and conceptual [58,67,71] approaches are valid for deriving satellite-derived observations of phytoplankton size structure in the Mediterranean Sea.

Both conceptual and empirical PSC models are abundance-based methods that infer phytoplankton size structure as a continuous function of total Chl-a concentration. When well trained, empirical approaches are not constrained by an underlying conceptual framework and often have a strong predictive power, are easy to implement and can be applied across broad temporal and spatial scales. On the other hand, conceptual models, whilst less flexible and potentially less predictive, offer ecologically meaningful model parameters and may be better suited for applications related to climate change [65]. Considering the

Remote Sens. 2025, 17, 2362 17 of 31

potential of the conceptual SST-dependent approach presented here, both in accounting for the effects of regional warming (SST) and in its applicability beyond the current ocean color record [67], we adopt this approach in the following section.

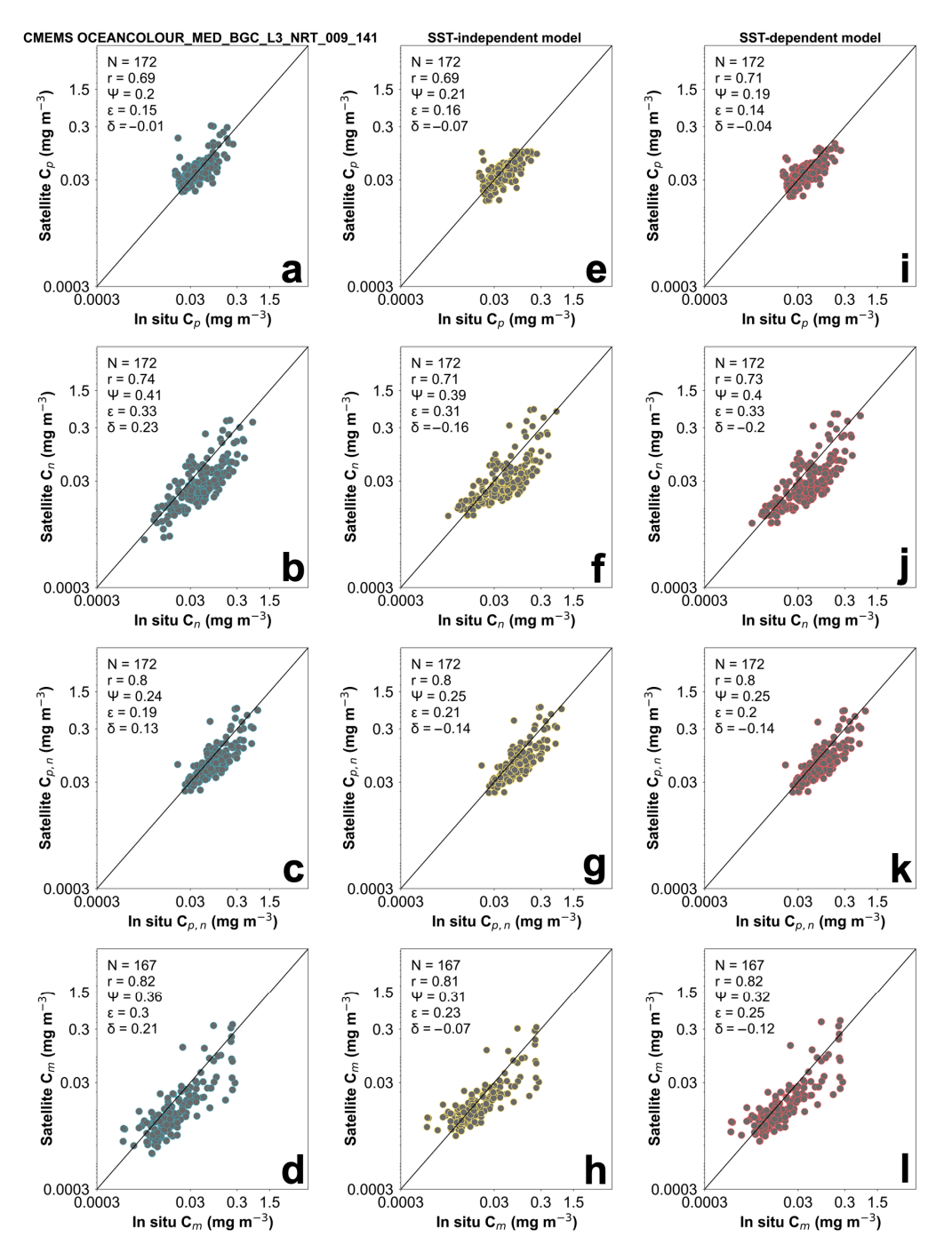


Figure 6. Model validation between in situ and satellite-derived size-fractionated Chl-a concentrations in the Mediterranean Sea. (\mathbf{a} – \mathbf{d}) Comparison of in situ size-fractionated Chl-a concentrations (C_p , C_n , $C_{p,n}$ and C_m) with satellite-derived values acquired from the regional Mediterranean ocean color dataset of the European Union Copernicus Marine Service online catalogue (OCEAN-COLOUR_MED_BGC_L3_NRT_009_141 [59–61]). The 1:1 line is shown as the solid black line. (\mathbf{e} – \mathbf{h}) As shown in (\mathbf{a} – \mathbf{d}) but with satellite-derived estimates of PSCs from the SST-independent three-component model. (\mathbf{i} – \mathbf{l}) As shown in panels (\mathbf{e} – \mathbf{h}) but incorporating the SST-dependency explained in Section 2.2.3.

3.5. Application of the Re-Parameterized Model to Satellite Ocean Color Data

To investigate whether long-term changes in phytoplankton size structure have occurred over the last three decades, we applied the validated, SST-dependent PSC model to remotely sensed estimates of total Chl-a concentration and computed annual trends for each phytoplankton size fraction spanning the period September 1997-July 2024 (Figure 7). The fraction of picophytoplankton (smaller cells) has increased across the majority of the Mediterranean Sea (Figure 7a), coinciding with a concurrent decrease in the nano-and micro-phytoplankton size fractions (Figure 7b,c). These relationships are statistically significant across the majority of the Eastern Mediterranean Sea, as well as parts of the Western Mediterranean, such as the Balearic and Tyrrhenian Seas. An exception is micro-phytoplankton, which exhibits significant trends primarily in the Eastern Mediterranean. These spatial trends are consistent with previous in situ studies that have reported shifts in community structure towards small-sized phytoplankton in numerous sub-regions of the Mediterranean Sea. For instance, the earlier study of Marty et al. [125] revealed an increasing trend in picophytoplankton over a 9-year period (1991–1999) due to a prolonged summer stratification period in the Ligurian Sea (Western Mediterranean, ~43.8°N, 8.8°E), based on in situ observations from the DYFAMED time-series station. In the northern Adriatic Sea (the Gulf of Trieste, ~45.7°N, 13.6°E), Mozetič et al. [146] observed a regime shift in 2002/2003, characterized by a decline in phytoplankton biomass and a switch to the predominance of a smaller phytoplankton size fraction (nanoflagellates). Ramirez-Romero et al. [139] reported a marked increase in small-sized phytoplankton in the Gulf of Tunis (~37.0°N, 10.5°E), driven by the combined effects of rising temperatures and increased anthropogenic nutrient input. Maugendre et al. [147] also reported a shift towards cyanobacteria under experimental warming in samples collected from the Bay of Villefranche (Northwest Mediterranean, ~43.7°N, 7.3°E).

At synoptic spatial scales, El Hourany et al. [22] used satellite-derived datasets to investigate the interannual variability of Mediterranean bioregions and their associated phytoplankton functional types and found an increasing prevalence of cyanobacteria, potentially linked with the ongoing warming trend observed in the basin. Similarly, the recent occurrence of Marine Heatwaves (MHWs) in the Mediterranean Sea has been associated with a shift in phytoplankton community structure to smaller cells [148,149]. These effects reflect broader, global patterns of shifts to smaller phytoplankton communities that flourish better in warmer, more stratified environments [137,150,151]. Aside from these general trends, interesting patterns can be observed within some of the notable mesoscale features of the Mediterranean. The Rhodes Gyre, a cyclonic eddy located in the Eastern Mediterranean (~30°E, 35°N), and often regarded as an "oasis" of biological productivity, exhibits a stronger trend of increasing picophytoplankton relative to the surrounding waters. In contrast, the adjacent anticyclonic Ierapetra Gyre, located just east of Crete, exhibits minimal trends. Whilst the trend in microphytoplankton is less pronounced, regions of increasing microphytoplankton contributions are evident in the North Adriatic and North Aegean Seas, as well as within the Lions Gyre (~5°E, 42°N). The reparameterized SST-dependent model framework presented here provides a suitable foundation for further satellite-based investigations into trends and long-term interannual variability in phytoplankton size structure, as well as their potential links to regional physical and climatic drivers.

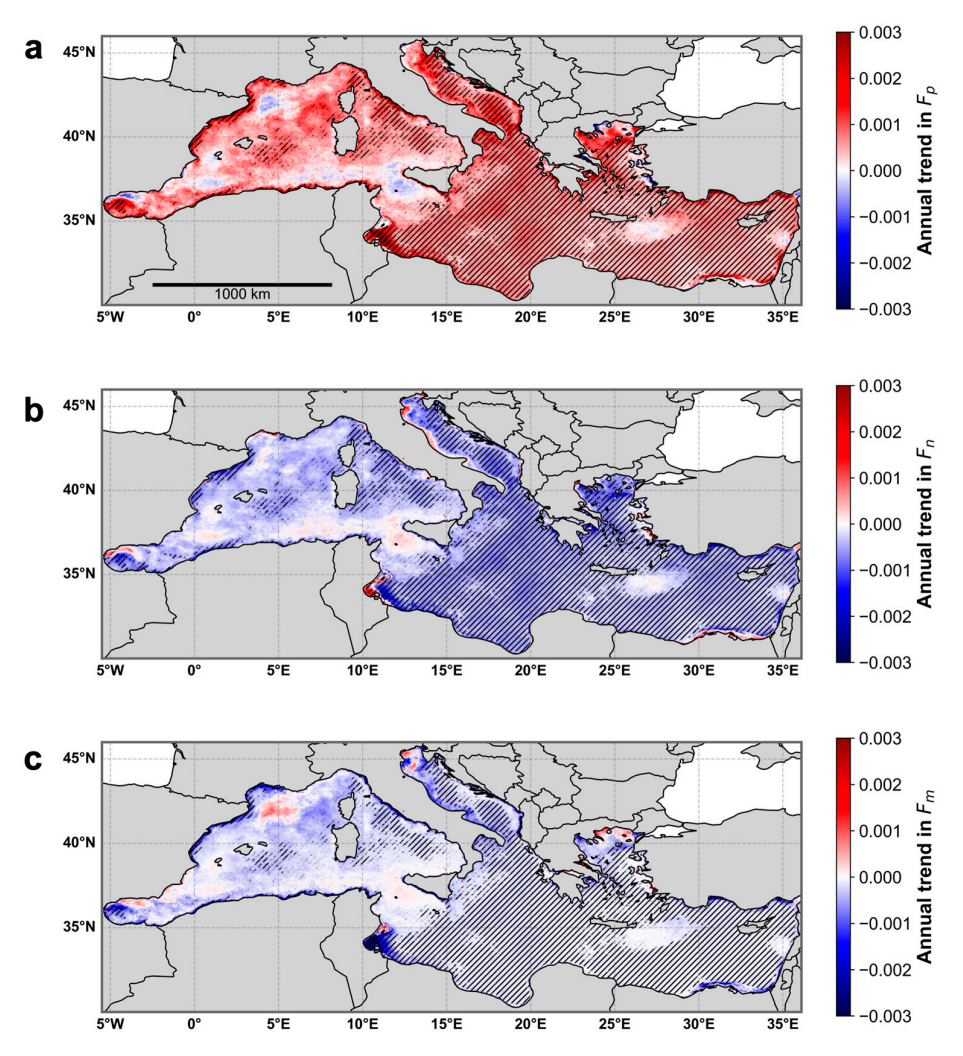


Figure 7. Annual trends in phytoplankton size fractions. Per-pixel trends, computed using linear regression analyses, for the picophytoplankton (F_p) (**a**), nanophytoplankton (F_n) (**b**) and microphytoplankton (F_m) (**c**) size fractions over the Mediterranean Sea. Size fractions were derived using the re-parameterized SST-dependent abundance-based phytoplankton size class model. We note that F_p , F_n and F_m represent the fractional contributions of the pico-, nano- and microplankton size classes to total chlorophyll-a (Chl-a) and are, therefore, dimensionless. The gray cross-hatching represents regions where p-values were statistically significant (p < 0.05).

3.6. Re-Evaluating In Situ Estimates of Phytoplankton Size Structure from Diagnostic Pigment Approaches

We utilized an extensive Mediterranean HPLC pigment dataset, acquired from various research cruise campaigns, to derive in situ estimates of phytoplankton size fractions that were used for the re-parameterization of the SST-independent and SST-dependent PSC models. Specifically, we followed the diagnostic pigment approach of Brewin et al. [58], which apportions some of 19′-hexanoyloxyfucoxanthin to picophytoplankton at low Chl-a concentrations, as this pigment can also be found in some pico-eukaryotes [152]. This approach has also been adopted in previous studies that have derived phytoplankton size fractions from HPLC pigment data [56,59]. Alternative datasets of phytoplankton size structure (e.g., acquired via size-fractionated filtration (SFF), flow cytometry or microscopy) are required to independently validate this diagnostic pigment approach and ascertain whether further adjustments are needed to account for the potential diversification of other pigments across different size classes. For example, a comparison between size-fractionated filtration (SFF) and HPLC (DPA)-derived size fractions in the Atlantic Ocean has revealed significant biases between the two methods [153], with HPLC-based DPA overestimating

Remote Sens. 2025, 17, 2362 20 of 31

nanophytoplankton chlorophyll and underestimating picophytoplankton chlorophyll when compared with SFF, even when 19′-hexanoyloxyfucoxanthin is apportioned to picophytoplankton at very low Chl-a concentrations. However, it should be acknowledged that the SFF method also has inherent uncertainties, with potential inaccuracies arising from filter pore size, clogging, phytoplankton cell breakage and the possibility that SFF may overestimate picoplankton contributions due to the increased cellular content of Chl-a per unit biomass of picophytoplankton cells [97,128,153]. Furthermore, observed differences between coincident datasets of phytoplankton size structure may not necessarily be systematic but potentially associated with the nature of the datasets themselves. In other words, differences may be regionally dependent, related to the considered depth range of the collected samples and/or dataset specific. For example, in Brewin et al. [71], the biases found using a different dataset (acquired from surface waters in the North Atlantic) were notably smaller, suggesting a reasonable agreement between the two methods.

The standard DPA approach allocates total chlorophyll-b, which is representative of both Prochlorococcus and Chlorophytes, to the picophytoplankton fraction, whereas 19'-hexanoyloxyfucoxanthin is typically attributed to nano-phytoplankton. However, photosynthetic Picoeukaryotes (PPEs) encompass a variety of taxa, including Prymnesiophytes, Pelagophytes and Chlorophytes, and can constitute significant components of picophytoplankton populations because of their larger biovolume and rapid growth rates compared to cyanobacteria [141]. Chlorophytes usually dominate PPE in nutrientrich, upwelling-influenced waters, whilst Prymnesiophytes and Pelagophytes have been shown to be an important component of the PPE assemblages in oligotrophic waters, as revealed by a variety of methods including plastid 16S rRNA gene sequencing and 18S rRNA gene sequencing of flow cytometry-sorted samples [154-157]. In the Eastern Mediterranean Sea, combined datasets from chemotaxonomic (CHEMTAX) analysis and flow cytometry-based cell counts showed that Pelagophytes belong entirely to picophytoplankton, while Prymnesiophytes can make up to 42% of total Chl-a attributed to PPEs [158]. These results also agree with carbon-based estimates from the EMS, where PPEs are found to dominate the picophytoplankton biomass within the surface layer of open-water stations, despite their significantly lower cell counts compared to cyanobacteria (Prochlorococcus and Synechococcus) [159]. Prymnesiophytes were also found to be the main picoeukaryotes that responded positively to a simulated dust deposition mesocosm experiment using EMS waters [160]. The results from a small-scale preliminary evaluation of 19'-hexanoyloxyfucoxanthin and total chlorophyll-b partitioning at a coastal site in the Eastern Mediterranean support the aforementioned observations (Figure S7). Approximately 65% of total 19'-hexanoyloxyfucoxanthin was attributed to the picophytoplankton fraction, with the remainder assigned to the nano-fraction (Figure S7). Similarly, around 50% of total chlorophyll-b was distributed equally between pico- and nano-phytoplankton. These findings highlight the potential need for modifications to the standard DPA approach.

Furthermore, nanoplanktonic diatoms such as *Minidiscus*, which predominantly contain the fucoxanthin pigment attributed to microphytoplankton, are known to contribute to the development of massive spring blooms in the Northwest Mediterranean [142]. Similarly, microscopic analyses of an interannual time series of phytoplankton size structure from the E1-M3A monitoring station, located north of Crete in the Eastern Mediterranean, revealed that ~80% (multiyear average) of detected photosynthetic dinoflagellates within the 0–20 m layer belonged to the nanoplanktonic size class (<20 μ m), with *Gymnodinium* spp. dominating the small (<20 μ m) dinoflagellates assemblage (Figure S8). Nanoplanktonic groups including prymesiophytes and chrysophytes are also known to contain fucoxanthin [97,115].

Remote Sens. 2025, 17, 2362 21 of 31

Given these findings, it is important to consider that further refinements to diagnostic pigment approaches applied to HPLC data may be necessary to account for the unique partitioning of pigments among phytoplankton groups in the Mediterranean Sea. A method for fucoxanthin partitioning between micro- and nano-phytoplankton was proposed by Devred et al. [115], which has been applied in recent studies on phytoplankton size structure [67,70,71]. Chase et al. [161] also proposed a series of modifications based on their comparisons between the traditional diagnostic pigment approach and flow cytometry. In their study, total chlorophyll-b was split equally between pico- and nanophytoplankton. Additionally, 50% of fucoxanthin and 75% of peridinin—both traditionally assigned solely to microphytoplankton—were attributed to nanophytoplankton, along with 19′-hexanoyloxyfucoxanthin and 19′-butanoyloxyfucoxanthin.

To assess whether adjustments to the diagnostic pigment approach (DPA) are worth consideration for future studies in the Mediterranean Sea, we re-computed phytoplankton size fractions from the HPLC dataset incorporating modified DPA equations based on the recommendations of Chase et al. [161] and the regional analyses presented here. Specifically, we assigned 50% of chlorophyll-b and 65% of 19'-hexanoyloxyfucoxanthin to picophytoplankton, and 75% of peridinin to nanophytoplankton, and divided fucoxanthin equally between micro- and nanophytoplankton (Equations (20)–(22)). The recalculated HPLC-derived size fractions were compared with concurrent measurements of size structure estimated from SFF, predominantly acquired in the oligotrophic waters of the Cretan Sea in the Eastern Mediterranean (see Section 2). Here, SFF measurements were limited to two broader size classes: picophytoplankton (0.2–2 μ m) and the combined nano- and micro-phytoplankton assemblage (>2 μ m). Thus, comparisons were only conducted for these two size classes.

$$F_p = \frac{(0.65W_3P_3 + 0.5W_6P_6 + W_7P_7)}{C_w} \tag{20}$$

$$F_n = \frac{(0.5W_1P_1 + 0.75W_2P_2 + 0.35W_3P_3 + W_4P_4 + W_5P_5 + 0.5W_6P_6)}{C_w}$$
(21)

$$F_m = \frac{(0.5W_1P_1 + 0.25W_2P_2)}{C_w} \tag{22}$$

Overall, the HPLC-derived size-fractionated Chl-a concentration estimates, calculated using the modified DPA (Equations (20)–(22)), show a significant improvement in alignment with concurrent SFF-based size structure estimates (Figure 8). For both size classes, the correlation coefficient between the datasets increased, while error metrics were similar or lower compared to size-fractionated Chl-a estimates derived from the traditional DPA previously applied in the Mediterranean Sea [56,59]. To verify whether the conceptual framework of the three-component model remains valid when incorporating the modifed DPA approach, we re-fitted the SST-independent model (Equations (8) and (9)) to in situ phytoplankton size fractions computed using Equations (20)–(22). The updated set of fixed model parameters ($C_p^m = 0.29 \text{ mg m}^{-3}$, $C_{p,n}^m = 6.62 \text{ mg m}^{-3}$, $D_p = 0.67 \text{ and}$ $D_{v,n} = 0.94$) exhibit some substantial differences (notably the markedly high value of $C_{v,n}^{m}$) due to the different apportioning of diagnostic pigments between size classes. Despite these changes, the re-parameterized three-component model, when fitted to the updated training dataset, still explains a similar level of variance in the in situ phytoplankton size fractions (F_p , F_n , $F_{p,n}$ and F_m) and size-specific Chl-a concentrations (C_p , C_n , $C_{p,n}$ and C_m) when plotted against total Chl-a concentration (Figure S9). Thus, even with potential future modifications to diagnostic pigment approaches in the Mediterranean Sea, the model framework presented here will likely remain a robust approach.

Remote Sens. 2025, 17, 2362 22 of 31

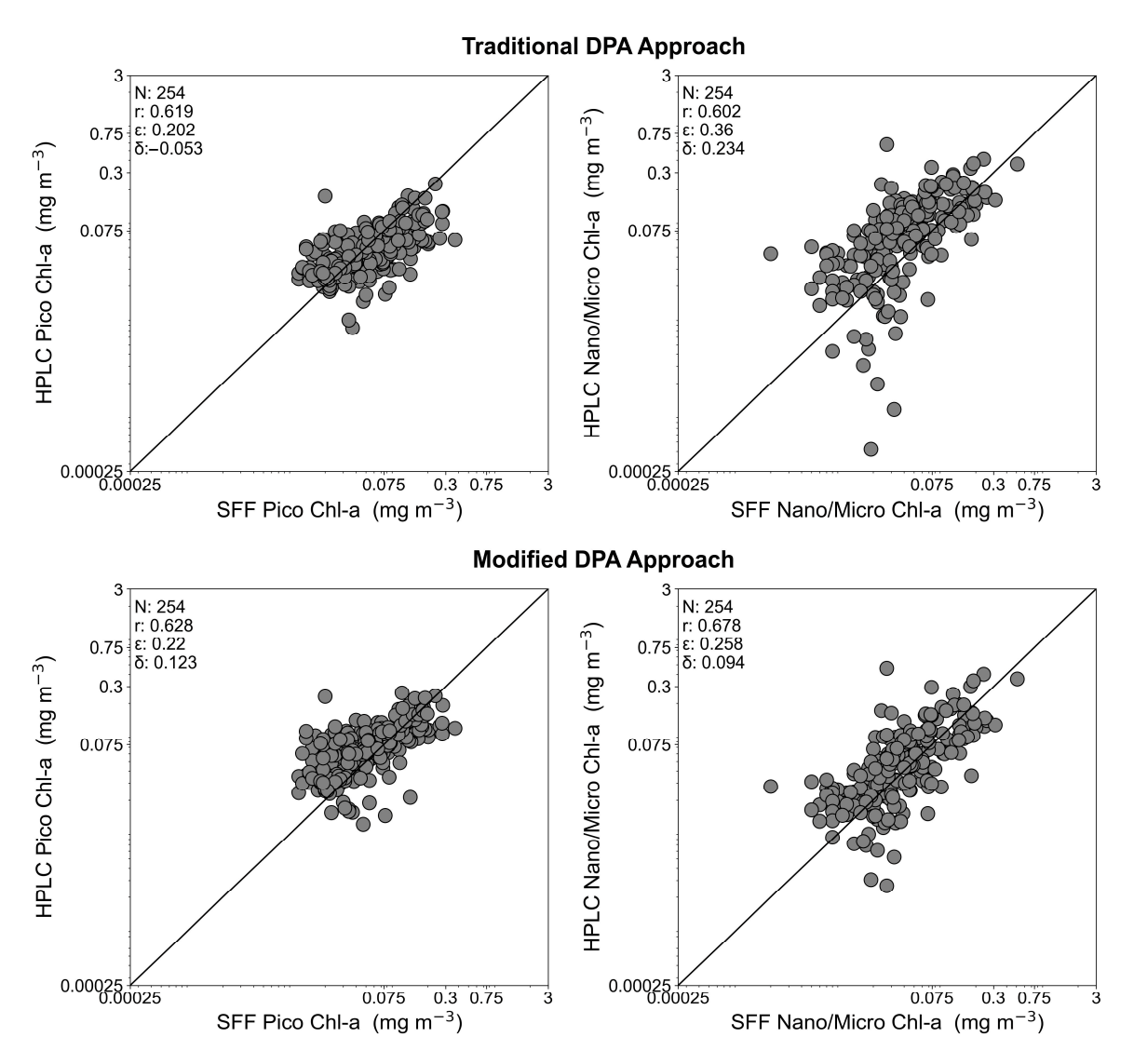


Figure 8. Comparison of size-fractionated Chl-a concentrations for picophytoplankton (<2 μ m) and the combined nano- and micro-phytoplankton (>2 μ m) assemblages, based on concurrent measurements of SFF and HPLC taken at the E1-M3A buoy station north of Crete Island (~35.736°N, 25.122°E). The 1:1 line is shown as the solid black line. Two different diagnostic pigment approaches were utilized for the computation of phytoplankton size fractions from the HPLC data.

It is worth noting that this comparison was based on samples acquired predominately in the Cretan Sea (Eastern Medierranean Sea), a typical oligotrophic system, exhibiting year-round low Chl-a concentrations (<0.2 mg m⁻³). However, we acknowledge that this comparison may not be representative of broader size–pigment relationships for the Western Mediterranean Sea; therefore, we highlight the necessity for further examination into how diagnostic pigments are allocated when deriving PSCs from pigment datasets. Furthermore, we re-emphasize the importance of incorporating multiple in situ approaches, such as SFF and flow cytometry, for the independent validation of PSCs and computation of measurement uncertainties [153,161]. Ultimately, such efforts provide the in situ framework from which satellite remote sensing approaches can be further developed and improved upon. Additionally, the model uses satellite-derived Chl-a concentration as its primary input. Therefore, accurate retrieval of Chl-a is essential—particularly in optically complex waters where Chl-a may not covary with colored dissolved organic matter (CDOM) or non-algal particles. While the regional algorithm used for Chl-a retrieval has demonstrated good performance in Case 2 waters of the Mediterranean Sea [60,61], the application of

Remote Sens. 2025, 17, 2362 23 of 31

the re-parameterized model in coastal or optically complex environments warrants careful consideration and further validation.

4. Conclusions

Using an updated HPLC pigment dataset representative of the Mediterranean Sea, we re-parameterized a conceptual, abundance-based PSC model that partitions phytoplankton biomass (as represented by the total Chl-a concentration) into three size classes: pico-, nano- and microphytoplankton. The re-parameterized model is able to effectively represent the ubiquitous relationships between total phytoplankton biomass and size structure, which have been documented across a wide range of oceanic environments. The parameters of the three-component model are known to be directly impacted by physical variables, such as light availability [70] and temperature [71]. Thus, a second, SST-dependent version of the re-parameterized model was proposed in this study. Independent, in situ validation of size-fractionated Chl-a concentrations demonstrated that the SST-dependent model exhibits an improved performance, with higher or comparable correlation coefficients and reduced error metrics, particularly for the retrieval of picophytoplankton.

Applying the validated SST-dependent model to remotely sensed ocean color observations demonstrated a strong correlation between satellite-derived estimates of phytoplankton size structure and concurrent in situ measurements. The SST-dependent model outperformed the conceptual SST-independent model and was comparable to the performance of the current operational ocean color dataset from the Copernicus Marine Data Store, which is based on the regional polynomial algorithms of Di Cicco et al. [59]. Per-pixel trend analyses, applied to long-term, satellite-derived phytoplankton size fractions revealed an increasing contribution of smaller phytoplankton across the broader Mediterranean Sea, accompanied by a decreasing contribution of nano- and micro-phytoplankton, supporting previous observations within the Mediterranean. Exceptions to this were found in notable mesoscale features, including semi-permanent gyres, whose characteristics and interannual variability warrant further investigation.

Building upon existing ocean color modeling frameworks [67,71], the conceptual PSC model presented in this study differs from prior statistical [59–61,114] and empirical [162] approaches by directly tying model parameters to the physical environment. This approach not only improves the retrieval of satellite-derived observations of phytoplankton size structure but can be carried forward into future studies on the response of phytoplankton ecological indicators to the continual warming trends of the Mediterranean Sea. Going forward, the recent launch of new hyperspectral satellite sensors dedicated to Earth observation, such as those onboard the NASA Plankton, Aerosol, Cloud, ocean Ecosystem (PACE) mission, along with methodological advancements in marine biodiversity assessment, such as Environmental DNA (eDNA) metabarcoding [163], offers unique opportunities to apply contemporary approaches for acquiring robust information on phytoplankton community structure. Given the basin's unique spatiotemporal variability of phytoplankton populations, which distinguishes it from other oligotrophic seas [8], we also emphasize that future research efforts should ideally be directed towards the acquisition of in situ pigment datasets and concurrent size-fractionated data, which would enable the refinement of existing diagnostic pigment approaches and further optimization of PSC models tailored for the Mediterranean Sea.

Supplementary Materials: The following supporting information can be downloaded at https: //www.mdpi.com/article/10.3390/rs17142362/s1. Figure S1: The ratio of total Chl-a concentration at the shallowest sampling depth to deeper vertical depths (up to 50 m) for each in situ sampling station. Figure S2: Measured total Chl-a concentration plotted against Chl-a computed by conducting a weighted sum of the diagnostic pigments (C_w). Figure S3: Comparison of HPLC-derived surface

Remote Sens. 2025, 17, 2362 24 of 31

total Chl-a concentrations from the independent validation dataset with concurrent, daily satellitederived matchups of total Chl-a concentration acquired from the Copernicus Marine Datastore (OCEANCOLOUR_MED_BGC_L3_NRT_009_141). Figure S4: Application of the three-component phytoplankton size class model to subsets of the $F_{p,n}$ training dataset, sorted by increasing sea surface temperature. Figure S5: Comparison of PSCs between in situ and modeled size-fractionated Chl-a concentrations based on the full training dataset. Figure S6: Radar plots comparing statistical error metrics for satellite-derived, size-specific chlorophyll-a (Chl-a) concentrations from the Copernicus operational dataset, the SST-independent model and the SST-dependent model. Figure S7: Allocation of 19'-hexanoyloxyfucoxanthin and total chlorophyll-b to total size-fractionated Chl-a concentrations in the Cretan Sea. Figure S8: Monthly time series of dinoflagellates, partitioned by size (>20 µm and <20 µm) based on optical microscopy measurements acquired at the POSEIDON E1-M3A buoy time series situated north of Crete (~35.736°N, 25.122°E). Figure S9: Fits of the re-parameterized threecomponent model to the HPLC training dataset computed using the modified diagnostic pigment approach. Table S1: Weights for the seven diagnostic pigments, obtained through multi-linear least squares regression, used in the diagnostic pigment analyses in Section 2.2.1, along with comparisons to relevant previous studies.

Author Contributions: Conceptualization, J.A.G., E.L., X.S., R.J.W.B. and D.E.R.; methodology, J.A.G., E.L., X.S., R.J.W.B. and D.E.R.; software, J.A.G. and E.L.; validation, J.A.G., E.L., A.D.C., V.E.B. and D.E.R.; formal analysis, J.A.G. and E.L.; investigation, J.A.G., E.L. and D.E.R.; data curation, J.A.G., E.L., S.P., M.M., A.P., A.D.C., V.E.B. and D.E.R.; writing—original draft preparation, J.A.G.; writing—review and editing, J.A.G., E.L., X.S., R.J.W.B., S.P., M.M., A.P., A.D.C., V.E.B. and D.E.R.; visualization, J.A.G. and E.L.; supervision, D.E.R.; project administration, D.E.R.; funding acquisition, J.A.G., E.L., X.S., R.J.W.B., A.D.C., V.E.B. and D.E.R. All authors have read and agreed to the published version of the manuscript.

Funding: This research was funded by the European Union HORIZON EUROPE program ACTNOW: Advancing understanding of Cumulative Impacts on European marine biodiversity, ecosystem functions and services for human wellbeing (Grant No. 101060072). J.A.G. was also funded by the European Space Agency Living Planet Fellowship (POSEIDON/14-03-2021). R.J.W.B. and X.S. were supported by a UK Research and Innovation Future Leader Fellowship (MR/V022792/1). E.L. acknowledges support by the Hellenic Foundation for Research and Innovation (H.F.R.I.) under the 2nd Call of "Research Projects to Support Faculty Members & Researchers" scheme (Programme OPTIMISE, Grant Number: 04808). V.E.B. and A.D.C. contributed to this work in the context of the Copernicus Marine Service (contract Refs. 21001L2-COP-TAC OC-2200 and 24251-COP TAC).

Data Availability Statement: A selection of the Mediterranean Sea in situ datasets on phytoplankton pigments are freely available from the following databases: SeaWiFS Bio-optical Archive and Storage System (SeaBASS, https://seabass.gsfc.nasa.gov/, accessed on 1 December 2024), MAREDAT global database of high performance liquid chromatography marine pigment measurements (https://doi.pangaea.de/10.1594/PANGAEA.793246) and the Oceanographic dataset in the Mediterranean Sea collected during the cruise BioArgoMed 2015 (https://www.seanoe.org/data/00405/51678/, accessed on 1 December 2024). Pigment datasets collected within the Eastern Mediterranean will be made available upon request by the authors. Satellite datasets of SST and ocean color are freely available from the Copernicus Marine Data Store (https://data.marine.copernicus.eu/products, accessed on 1 December 2024).

Acknowledgments: We gratefully acknowledge the Copernicus Marine Service for providing the satellite datasets used in this study. We also sincerely thank the researchers, technicians, data managers, captains and crews of all the research vessels and mooring stations presented here, whose contributions to this study were essential.

Conflicts of Interest: The authors declare no conflicts of interest.

Remote Sens. 2025, 17, 2362 25 of 31

References

1. Bethoux, J.P.; Gentili, B.; Morin, P.; Nicolas, E.; Pierre, C.; Ruiz-Pino, D. The Mediterranean Sea: A Miniature Ocean for Climatic and Environmental Studies and a Key for the Climatic Functioning of the North Atlantic. *Prog. Oceanogr.* 1999, 44, 131–146. [CrossRef]

- 2. D'Ortenzio, F.; D'Alcalà, M.R. On the Trophic Regimes of the Mediterranean Sea: A Satellite Analysis. *Biogeosciences* **2009**, *6*, 139–148. [CrossRef]
- 3. Skliris, N. Past, Present and Future Patterns of the Thermohaline Circulation and Characteristic Water Masses of the Mediterranean Sea. In *The Mediterranean Sea: Its History and Present Challenges*; Springer: Dordrecht, The Netherlands, 2014; pp. 29–48. [CrossRef]
- 4. Berland, B.; Bonin, D.; Maestrini, S.Y. Azote ou phosphore? Considérations sur le paradoxe nutritionnel de la mer Méditerranée. *Oceanol. Acta* **1980**, *3*, 135–141.
- 5. Krom, M.D.; Kress, N.; Brenner, S.; Gordon, L.I. Phosphorus Limitation of Primary Productivity in the Eastern Mediterranean Sea. *Limnol. Oceanogr.* **1991**, *36*, 424–432. [CrossRef]
- 6. Antoine, D.; Morel, A.; Andre, J.M. Algal Pigment Distribution and Primary Production in the Eastern Mediterranean as Derived from Coastal Zone Color Scanner Observations. *J. Geophys. Res. Oceans* **1995**, *100*, 16193–16209. [CrossRef]
- 7. Lazzari, P.; Solidoro, C.; Salon, S.; Bolzon, G. Spatial Variability of Phosphate and Nitrate in the Mediterranean Sea: A Modeling Approach. *Deep Sea Res. I Oceanogr. Res. Pap.* **2016**, *108*, 39–52. [CrossRef]
- 8. Siokou-Frangou, I.; Christaki, U.; Mazzocchi, M.G.; Montresor, M.; Ribera D'Alcala, M.; Vaque, D.; Zingone, A. Plankton in the Open Mediterranean Sea: A Review. *Biogeosciences* **2010**, *7*, 1543–1586. [CrossRef]
- 9. Macias, D.; Garcia-Gorriz, E.; Stips, A. Major Fertilization Sources and Mechanisms for Mediterranean Sea Coastal Ecosystems. *Limnol. Oceanogr.* **2018**, *63*, 897–914. [CrossRef]
- 10. Kalloniati, K.; Christou, E.D.; Kournopoulou, A.; Gittings, J.A.; Theodorou, I.; Zervoudaki, S.; Raitsos, D.E. Long-Term Warming and Human-Induced Plankton Shifts at a Coastal Eastern Mediterranean Site. *Sci. Rep.* **2023**, *13*, 21068. [CrossRef]
- 11. Estrada, M. Primary production in the Northwestern Mediterranean. Eur. Anchovy Environ. 1996, 60, 55–64.
- 12. Sabatés, A.; Olivar, M.P.; Salat, J.; Palomera, I.; Alemany, F. Physical and Biological Processes Controlling the Distribution of Fish Larvae in the NW Mediterranean. *Prog. Oceanogr.* **2007**, *74*, 355–376. [CrossRef]
- 13. Lejeusne, C.; Chevaldonné, P.; Pergent-Martini, C.; Boudouresque, C.F.; Pérez, T. Climate Change Effects on a Miniature Ocean: The Highly Diverse, Highly Impacted Mediterranean Sea. *Trends Ecol. Evol.* **2010**, 25, 250–260. [CrossRef] [PubMed]
- 14. Friedrich, R.G.A.; Haarer, J.; Ibm, H.J.; Bethoux, J.; Gentili, B.; Raunet, J.; Tailliez, D. Warming Trend in the Western Mediterranean Deep Water. *Nature* **1990**, *347*, 660–662. [CrossRef]
- 15. Nykjaer, L. Mediterranean Sea Surface Warming 1985–2006. Clim. Res. 2009, 39, 11–17. [CrossRef]
- 16. Raitsos, D.E.; Beaugrand, G.; Georgopoulos, D.; Zenetos, A.; Pancucci-Papadopoulou, A.M.; Theocharis, A.; Papathanassiou, E. Global Climate Change Amplifies the Entry of Tropical Species into the Eastern Mediterranean Sea. *Limnol. Oceanogr.* **2010**, *55*, 1478–1484. [CrossRef]
- 17. Mohamed, B.; Abdallah, A.M.; Alam El-Din, K.; Nagy, H.; Shaltout, M. Inter-Annual Variability and Trends of Sea Level and Sea Surface Temperature in the Mediterranean Sea over the Last 25 Years. *Pure Appl. Geophys.* **2019**, *176*, 3787–3810. [CrossRef]
- 18. Pastor, F.; Valiente, J.A.; Khodayar, S. A Warming Mediterranean: 38 Years of Increasing Sea Surface Temperature. *Remote Sens.* **2020**, *12*, 2687. [CrossRef]
- 19. Pisano, A.; Marullo, S.; Artale, V.; Falcini, F.; Yang, C.; Leonelli, F.E.; Santoleri, R.; Nardelli, B.B. New Evidence of Mediterranean Climate Change and Variability from Sea Surface Temperature Observations. *Remote Sens.* **2020**, *12*, 132. [CrossRef]
- 20. Giorgi, F. Climate Change Hot-Spots. Geophys. Res. Lett. 2006, 33, 8707. [CrossRef]
- 21. Tuel, A.; Eltahir, E.A.B. Why Is the Mediterranean a Climate Change Hot Spot? J. Clim. 2020, 33, 5829–5843. [CrossRef]
- 22. El Hourany, R.; Mejia, C.; Faour, G.; Crépon, M.; Thiria, S. Evidencing the Impact of Climate Change on the Phytoplankton Community of the Mediterranean Sea Through a Bioregionalization Approach. *J. Geophys. Res. Oceans* **2021**, *126*, e2020JC016808. [CrossRef]
- 23. Cabrerizo, M.J.; Medina-Sánchez, J.M.; González-Olalla, J.M.; Sánchez-Gómez, D.; Carrillo, P. Microbial plankton responses to multiple environmental drivers in marine ecosystems with different phosphorus limitation degrees. *Sci. Total Environ.* **2022**, *816*, 151491. [CrossRef] [PubMed]
- 24. Soulié, T.; Vidussi, F.; Courboulès, J.; Mas, S.; Mostajir, B. Metabolic Responses of Plankton to Warming during Different Productive Seasons in Coastal Mediterranean Waters Revealed by In Situ Mesocosm Experiments. *Sci. Rep.* **2022**, *12*, 9001. [CrossRef]
- 25. Soulié, T.; Vidussi, F.; Mas, S.; Mostajir, B. Functional and Structural Responses of Plankton Communities toward Consecutive Experimental Heatwaves in Mediterranean Coastal Waters. *Sci. Rep.* **2023**, *13*, 8050. [CrossRef]
- Deserti, M.; Cacciamani, C.; Chiggiato, J.; Rinaldi, A.; Ferrari, C.R. Relationships between Northern Adriatic Sea Mucilage Events and Climate Variability. Sci. Total Environ. 2005, 353, 82–88. [CrossRef]

Remote Sens. 2025, 17, 2362 26 of 31

27. Molinero, J.C.; Ibanez, F.; Souissi, S.; Buecher, E.; Dallot, S.; Nival, P. Climate Control on the Long-Term Anomalous Changes of Zooplankton Communities in the Northwestern Mediterranean. *Glob. Change Biol.* **2008**, *14*, 11–26. [CrossRef]

- 28. Vergés, A.; Tomas, F.; Cebrian, E.; Ballesteros, E.; Kizilkaya, Z.; Dendrinos, P.; Karamanlidis, A.A.; Spiegel, D.; Sala, E. Tropical rabbitfish and the deforestation of a warming temperate sea. *J. Ecol.* **2014**, *102*, 1518–1527. [CrossRef]
- 29. Vasilakopoulos, P.; Raitsos, D.E.; Tzanatos, E.; Maravelias, C.D. Resilience and Regime Shifts in a Marine Biodiversity Hotspot. *Sci. Rep.* **2017**, *7*, 13647. [CrossRef]
- 30. Christidis, G.; Mandalakis, M.; Anastasiou, T.I.; Tserpes, G.; Peristeraki, P.; Somarakis, S. Keeping Lagocephalus Sceleratus off the Table: Sources of Variation in the Quantity of Ttx, Ttx Analogues, and Risk of Tetrodotoxication. *Toxins* **2021**, *13*, 896. [CrossRef]
- 31. Coll, M.; Albo-Puigserver, M.; Navarro, J.; Palomera, I.; Dambacher, J.M. Who Is to Blame? Plausible Pressures on Small Pelagic Fish Population Changes in the Northwestern Mediterranean Sea. *Mar. Ecol. Prog. Ser.* **2019**, *617–618*, 277–294. [CrossRef]
- 32. Maynou, F.; Sabatés, A.; Salat, J. Clues from the Recent Past to Assess Recruitment of Mediterranean Small Pelagic Fishes under Sea Warming Scenarios. *Clim. Change* **2014**, *126*, 175–188. [CrossRef]
- 33. Moltó, V.; Palmer, M.; Ospina-Álvarez, A.; Pérez-Mayol, S.; Benseddik, A.B.; Gatt, M.; Morales-Nin, B.; Alemany, F.; Catalán, I.A. Projected Effects of Ocean Warming on an Iconic Pelagic Fish and Its Fishery. *Sci. Rep.* **2021**, *11*, 8803. [CrossRef]
- 34. Tzanatos, E.; Raitsos, D.E.; Triantafyllou, G.; Somarakis, S.; Tsonis, A.A. Indications of a Climate Effect on Mediterranean Fisheries. *Clim. Change* **2014**, 122, 41–54. [CrossRef]
- 35. Darmaraki, S.; Denaxa, D.; Theodorou, I.; Livanou, E.; Rigatou, D.; Raitsos, D.E.; Stavrakidis-Zachou, O.; Dimarchopoulou, D.; Bonino, G.; McAdam, R.; et al. Marine Heatwaves in the Mediterranean Sea: A Literature Review. *Mediterr. Mar. Sci.* 2024, 25, 586–620. [CrossRef]
- 36. Longhurst, A.; Sathyendranath, S.; Platt, T.; Caverhill, C. An Estimate of Global Primary Production in the Ocean from Satellite Radiometer Data. *J. Plankton Res.* **1995**, *17*, 1245–1271. [CrossRef]
- 37. Field, C.B.; Behrenfeld, M.J.; Randerson, J.T.; Falkowski, P. Primary Production of the Biosphere: Integrating Terrestrial and Oceanic Components. *Science* 1998, 281, 237–240. [CrossRef]
- 38. Brewin, R.J.W.; Sathyendranath, S.; Platt, T.; Bouman, H.; Ciavatta, S.; Dall'Olmo, G.; Dingle, J.; Groom, S.; Jönsson, B.; Kostadinov, T.S.; et al. Sensing the Ocean Biological Carbon Pump from Space: A Review of Capabilities, Concepts, Research Gaps and Future Developments. *Earth Sci. Rev.* **2021**, *217*, 103604. [CrossRef]
- 39. Niemi, G.J.; McDonald, M.E. Application of Ecological Indicators. Annu. Rev. Ecol. Evol. Syst. 2004, 35, 89–111. [CrossRef]
- 40. Racault, M.F.; Platt, T.; Sathyendranath, S.; Ağirbaş, E.; Martinez Vicente, V.; Brewin, R. Plankton Indicators and Ocean Observing Systems: Support to the Marine Ecosystem State Assessment. *J. Plankton Res.* **2014**, *36*, 621–629. [CrossRef]
- 41. Platt, T.; Sathyendranath, S. Ecological Indicators for the Pelagic Zone of the Ocean from Remote Sensing. *Remote Sens. Environ.* **2008**, 112, 3426–3436. [CrossRef]
- 42. Chisholm, S.W. Phytoplankton size. In *Primary Productivity and Biogeochemical Cycles in the Sea*; Platt, T., Li, W.K.W., Eds.; Springer: New York, NY, USA, 1992; pp. 213–237. [CrossRef]
- 43. McCave, I.N. Vertical Flux of Particles in the Ocean. Deep Sea Res. Oceanogr. Abstr. 1975, 22, 491–502. [CrossRef]
- 44. Eppley, R.W.; Peterson, B.J. Particulate Organic Matter Flux and Planktonic New Production in the Deep Ocean. *Nature* **1979**, 282, 677–680. [CrossRef]
- 45. Briggs, N.; Perry, M.J.; Cetinić, I.; Lee, C.; D'Asaro, E.; Gray, A.M.; Rehm, E. High-Resolution Observations of Aggregate Flux during a Sub-Polar North Atlantic Spring Bloom. *Deep Sea Res. Part I Oceanogr. Res. Pap.* **2011**, *58*, 1031–1039. [CrossRef]
- 46. Mouw, C.B.; Barnett, A.; McKinley, G.A.; Gloege, L.; Pilcher, D. Phytoplankton Size Impact on Export Flux in the Global Ocean. *Global Biogeochem. Cycles* **2016**, *30*, 1542–1562. [CrossRef]
- 47. Henson, S.A.; Laufkötter, C.; Leung, S.; Giering, S.L.C.; Palevsky, H.I.; Cavan, E.L. Uncertain Response of Ocean Biological Carbon Export in a Changing World. *Nat. Geosci.* **2022**, *15*, 248–254. [CrossRef]
- 48. Legendre, L.; Le Fèvre, J. From Individual Plankton Cells to Pelagic Marine Ecosystems and to Global Biogeochemical Cycles. In *Particle Analysis in Oceanography*; Springer: Berlin/Heidelberg, Germany, 1991; pp. 261–300. [CrossRef]
- 49. Moloney, C.L.; Field, J.G. The Size-Based Dynamics of Plankton Food Webs. I. A Simulation Model of Carbon and Nitrogen Flows. *J. Plankton Res.* **1991**, *13*, 1003–1038. [CrossRef]
- 50. Finkel, Z.V. Does Phytoplankton Cell Size Matter? The Evolution of Modern Marine Food Webs. In *Evolution of Primary Producers in the Sea*; Falkowski, P.G., Knoll, A.H., Eds.; Academic Press: Cambridge, MA, USA, 2007; pp. 333–350. [CrossRef]
- 51. Sathyendranath, S. (Ed.) *Phytoplankton Functional Types from Space*; IOCCG Report 15; International Ocean Colour Coordinating Group: Dartmouth, NS, Canada, 2014; p. 156.
- 52. Navarro, G.; Alvain, S.; Vantrepotte, V.; Huertas, I.E. Identification of Dominant Phytoplankton Functional Types in the Mediterranean Sea Based on a Regionalized Remote Sensing Approach. *Remote Sens. Environ.* **2014**, *152*, *557–575*. [CrossRef]
- 53. Navarro, G.; Almaraz, P.; Caballero, I.; Vázquez, Á.; Huertas, I.E. Reproduction of Spatio-Temporal Patterns of Major Mediterranean Phytoplankton Groups from Remote Sensing OC-CCI Data. Front. Mar. Sci. 2017, 4, 266825. [CrossRef]

Remote Sens. 2025, 17, 2362 27 of 31

54. Alvain, S.; Moulin, C.; Dandonneau, Y.; Bréon, F.M. Remote Sensing of Phytoplankton Groups in Case 1 Waters from Global SeaWiFS Imagery. *Deep Sea Res. Part I Oceanogr. Res. Pap.* **2005**, *52*, 1989–2004. [CrossRef]

- 55. Alvain, S.; Moulin, C.; Dandonneau, Y.; Loisel, H. Seasonal Distribution and Succession of Dominant Phytoplankton Groups in the Global Ocean: A Satellite View. *Global Biogeochem. Cycles* **2008**, 22, GB3001. [CrossRef]
- 56. Sammartino, M.; Di Cicco, A.; Marullo, S.; Santoleri, R. Spatio-Temporal Variability of Micro-, Nano- and Pico-Phytoplankton in the Mediterranean Sea from Satellite Ocean Colour Data of SeaWiFS. *Ocean Sci.* **2015**, *11*, 759–778. [CrossRef]
- 57. Brewin, R.J.W.; Devred, E.; Sathyendranath, S.; Lavender, S.J.; Hardman-Mountford, N.J. Model of Phytoplankton Absorption Based on Three Size Classes. *Appl. Opt.* **2011**, *50*, 4535–4549. [CrossRef] [PubMed]
- 58. Brewin, R.J.W.; Sathyendranath, S.; Hirata, T.; Lavender, S.J.; Barciela, R.M.; Hardman-Mountford, N.J. A Three-Component Model of Phytoplankton Size Class for the Atlantic Ocean. *Ecol. Modell.* **2010**, 221, 1472–1483. [CrossRef]
- Di Cicco, A.; Sammartino, M.; Marullo, S.; Santoleri, R. Regional Empirical Algorithms for an Improved Identification of Phytoplankton Functional Types and Size Classes in the Mediterranean Sea Using Satellite Data. Front. Mar. Sci. 2017, 4, 254855.
 [CrossRef]
- 60. Brando, V.E.; Santoleri, R.; Colella, S.; Volpe, G.; Di Cicco, A.; Sammartino, M.; González Vilas, L.; Lapucci, C.; Böhm, E.; Zoffoli, M.L.; et al. Overview of Operational Global and Regional Ocean Colour Essential Ocean Variables Within the Copernicus Marine Service. *Remote Sens.* 2024, 16, 4588. [CrossRef]
- 61. Colella, S.; Brando, V.E.; Di Cicco, A.; D'Alimonte, D.; Forneris, V.; Bracaglia, M. Quality Information Document for Ocean Colour Mediterranean and Black Sea Observation Product Release 4.0; Mercator Ocean International: Toulouse, France, 2024. [CrossRef]
- 62. El Hourany, R.; Abboud-Abi Saab, M.; Faour, G.; Mejia, C.; Crépon, M.; Thiria, S. Phytoplankton Diversity in the Mediterranean Sea From Satellite Data Using Self-Organizing Maps. *J. Geophys. Res. Oceans* **2019**, *124*, 5827–5843. [CrossRef]
- 63. Bracher, A.; Bouman, H.A.; Brewin, R.J.W.; Bricaud, A.; Brotas, V.; Ciotti, A.M.; Clementson, L.; Devred, E.; Di Cicco, A.; Dutkiewicz, S.; et al. Obtaining Phytoplankton Diversity from Ocean Color: A Scientific Roadmap for Future Development. *Front. Mar. Sci.* 2017, 4, 245888. [CrossRef]
- 64. Morel, A.; Prieur, L. Analysis of Variations in Ocean Color. Limnol. Oceanogr. 1977, 22, 709–722. [CrossRef]
- 65. Sathyendranath, S.; Brewin, R.J.W.; Jackson, T.; Mélin, F.; Platt, T. Ocean-Colour Products for Climate-Change Studies: What Are Their Ideal Characteristics? *Remote Sens. Environ.* **2017**, 203, 125–138. [CrossRef]
- 66. Brewin, R.J.W.; Morán, X.A.G.; Raitsos, D.E.; Gittings, J.A.; Calleja, M.L.; Viegas, M.; Ansari, M.I.; Al-Otaibi, N.; Huete-Stauffer, T.M.; Hoteit, I. Factors Regulating the Relationship Between Total and Size-Fractionated Chlorophyll-a in Coastal Waters of the Red Sea. Front. Microbiol. 2019, 10, 472071. [CrossRef]
- 67. Sun, X.; Brewin, R.J.W.; Sathyendranath, S.; Dall'Olmo, G.; Airs, R.; Barlow, R.; Bracher, A.; Brotas, V.; Kheireddine, M.; Lamont, T.; et al. Coupling Ecological Concepts with an Ocean-Colour Model: Phytoplankton Size Structure. *Remote Sens. Environ.* 2023, 285, 113415. [CrossRef]
- 68. Brewin, R.J.W.; Hardman-Mountford, N.J.; Lavender, S.J.; Raitsos, D.E.; Hirata, T.; Uitz, J.; Devred, E.; Bricaud, A.; Ciotti, A.; Gentili, B. An Intercomparison of Bio-Optical Techniques for Detecting Dominant Phytoplankton Size Class from Satellite Remote Sensing. *Remote Sens. Environ.* **2011**, *115*, 325–339. [CrossRef]
- 69. Brewin, R.J.W.; Sathyendranath, S.; Tilstone, G.; Lange, P.K.; Platt, T. A Multicomponent Model of Phytoplankton Size Structure. *J. Geophys. Res. Oceans* **2014**, *119*, 3478–3496. [CrossRef]
- 70. Brewin, R.J.W.; Sathyendranath, S.; Jackson, T.; Barlow, R.; Brotas, V.; Airs, R.; Lamont, T. Influence of Light in the Mixed-Layer on the Parameters of a Three-Component Model of Phytoplankton Size Class. *Remote Sens. Environ.* **2015**, *168*, 437–450. [CrossRef]
- 71. Brewin, R.J.W.; Ciavatta, S.; Sathyendranath, S.; Jackson, T.; Tilstone, G.; Curran, K.; Airs, R.L.; Cummings, D.; Brotas, V.; Organelli, E.; et al. Uncertainty in Ocean-Color Estimates of Chlorophyll for Phytoplankton Groups. *Front. Mar. Sci.* 2017, 4, 254350. [CrossRef]
- 72. Brewin, R.J.W.; Tilstone, G.H.; Jackson, T.; Cain, T.; Miller, P.I.; Lange, P.K.; Misra, A.; Airs, R.L. Modelling Size-Fractionated Primary Production in the Atlantic Ocean from Remote Sensing. *Prog. Oceanogr.* **2017**, *158*, 130–149. [CrossRef]
- 73. Brotas, V.; Brewin, R.J.W.; Sá, C.; Brito, A.C.; Silva, A.; Mendes, C.R.; Diniz, T.; Kaufmann, M.; Tarran, G.; Groom, S.B.; et al. Deriving Phytoplankton Size Classes from Satellite Data: Validation along a Trophic Gradient in the Eastern Atlantic Ocean. *Remote Sens. Environ.* **2013**, 134, 66–77. [CrossRef]
- 74. Corredor-Acosta, A.; Morales, C.E.; Brewin, R.J.W.; Auger, P.A.; Pizarro, O.; Hormazabal, S.; Anabalón, V. Phytoplankton Size Structure in Association with Mesoscale Eddies off Central-Southern Chile: The Satellite Application of a Phytoplankton Size-Class Model. *Remote Sens.* 2018, 10, 834. [CrossRef]
- 75. Lamont, T.; Barlow, R.G.; Brewin, R.J.W. Variations in Remotely-Sensed Phytoplankton Size Structure of a Cyclonic Eddy in the Southwest Indian Ocean. *Remote Sens.* **2018**, *10*, 1143. [CrossRef]
- 76. Lin, J.; Cao, W.; Wang, G.; Hu, S. Satellite-Observed Variability of Phytoplankton Size Classes Associated with a Cold Eddy in the South China Sea. *Mar. Pollut. Bull.* **2014**, *83*, 190–197.

Remote Sens. 2025, 17, 2362 28 of 31

77. Sahay, A.; Ali, S.M.; Gupta, A.; Goes, J.I. Ocean Color Satellite Determinations of Phytoplankton Size Class in the Arabian Sea during the Winter Monsoon. *Remote Sens. Environ.* **2017**, 198, 286–296. [CrossRef]

- 78. Liu, X.; Devred, E.; Johnson, C. Remote Sensing of Phytoplankton Size Class in Northwest Atlantic from 1998 to 2016: Bio-Optical Algorithms Comparison and Application. *Remote Sens.* **2018**, *10*, 1028. [CrossRef]
- 79. Sun, X.; Shen, F.; Brewin, R.J.W.; Liu, D.; Tang, R. Twenty-Year Variations in Satellite-Derived Chlorophyll-a and Phytoplankton Size in the Bohai Sea and Yellow Sea. *J. Geophys. Res. Oceans* **2019**, *124*, 8887–8912. [CrossRef]
- 80. Sun, X.; Shen, F.; Liu, D.; Bellerby, R.G.J.; Liu, Y.; Tang, R. In Situ and Satellite Observations of Phytoplankton Size Classes in the Entire Continental Shelf Sea, China. *J. Geophys. Res. Oceans* **2018**, *123*, 3523–3544. [CrossRef]
- 81. Gittings, J.A.; Brewin, R.J.W.; Raitsos, D.E.; Kheireddine, M.; Ouhssain, M.; Jones, B.H.; Hoteit, I. Remotely Sensing Phytoplankton Size Structure in the Red Sea. *Remote Sens. Environ.* **2019**, 234, 111387. [CrossRef]
- 82. Gittings, J.A.; Raitsos, D.E.; Brewin, R.J.; Hoteit, I. Links between Phenology of Large Phytoplankton and Fisheries in the Northern and Central Red Sea. *Remote Sens.* **2021**, *13*, 231. [CrossRef]
- 83. Turner, K.J.; Mouw, C.B.; Hyde, K.J.W.; Morse, R.; Ciochetto, A.B. Optimization and Assessment of Phytoplankton Size Class Algorithms for Ocean Color Data on the Northeast U.S. Continental Shelf. *Remote Sens. Environ.* **2021**, 267, 112729. [CrossRef]
- 84. Werdell, P.J.; Bailey, S.; Fargion, G.; Pietras, C.; Knobelspiesse, K.; Feidman, G.; McClain, C. Unique Data Repository Facilitates Ocean Color Satellite Validation. *Eos, Trans. Am. Geophys. Union* **2003**, *84*, 377–387. [CrossRef]
- 85. Claustre, H.; Antoine, D.; Babin, M.; Belviso, S.; Begovic, M.; Bianchi, M.; Birdwhistell, S.; Blanchot, J.; Bricaud, A.; Bruyant, F.; et al. BIOGEOCHEMICAL Dataset Collected During the PROSOPE Cruise. Available online: https://www.seanoe.org/data/00 605/71723/ (accessed on 1 December 2024).
- 86. Antoine, D.; Chami, M.; Claustre, H.; d'Ortenzio, F.; Morel, A.; Becu, G.; Gentili, B.; Louis, F.; Ras, J.; Roussier, E.; et al. BOUSSOLE: A Joint CNRS-INSU, ESA, CNES, and NASA Ocean Color Calibration and Validation Activity; Goddard Space Flight Center: Greenbelt, MD, USA, 2006.
- 87. Behrenfeld, M.; Dall'Olmo, G. BOUM08 HLPC Dataset. 2021. Available online: https://seabass.gsfc.nasa.gov/archive/OSU/VF/archive (accessed on 1 December 2024).
- 88. Peloquin, J.; Swan, C.; Gruber, N.; Vogt, M.; Claustre, H.; Ras, J.; Uitz, J.; Barlow, R.; Behrenfeld, M.; Bidigare, R.; et al. The MAREDAT Global Database of High Performance Liquid Chromatography Marine Pigment Measurements. *Earth Syst. Sci. Data* **2013**, *5*, 109–123. [CrossRef]
- 89. Prieur, L. ALMOFRONT 2—LEG 2 Cruise, RV L'Atalante. 1997. Available online: https://campagnes.flotteoceanographique.fr/campagnes/97010132/. (accessed on 1 December 2024).
- 90. Prieur, L. ALMOFRONT.LEG2 Cruise, RV L'Atalante. 1991. Available online: https://campagnes.flotteoceanographique.fr/campagnes/91004212/ (accessed on 1 December 2024).
- 91. Raimbault, P. MTPII-MATER/MINOS MAY96 Cruise, RV Le Suroît. 1996. Available online: https://campagnes.flotteoceanographique.fr/campagnes/96020030/ (accessed on 1 December 2024).
- 92. Vidussi, F.; Claustre, H.; Manca, B.B.; Luchetta, A.; Marty, J.C. Phytoplankton Pigment Distribution in Relation to Upper Thermocline Circulation in the Eastern Mediterranean Sea during Winter. *J. Geophys. Res. Oceans* **2001**, *106*, 19939–19956. [CrossRef]
- 93. Chiaverini, J. DYFAMED. 1987. Available online: https://campagnes.flotteoceanographique.fr/series/89/ (accessed on 1 December 2024).
- 94. Taillandier, V.; Wagener, T.; D'Ortenzio, F.; Mayot, N.; Legoff, H.; Ras, J.; Coppola, L.; Pasqueron de Fommervault, O.; Bittig, H.; Lefevre, D.; et al. Oceanographic Dataset in the Mediterranean Sea Collected During the Cruise BioArgoMed. 2021. Available online: https://www.seanoe.org/data/00405/51678/ (accessed on 1 December 2024).
- 95. Livanou, E.; Sauzède, R.; Psarra, S.; Mandalakis, M.; Dall'Olmo, G.; Brewin, R.J.W.; Raitsos, D.E. Evaluating MULTIOBS Chlorophyll-a with Ground-Truth Observations in the Eastern Mediterranean Sea. *Remote Sens.* **2024**, *16*, 4705. [CrossRef]
- 96. Livanou, E.; Lagaria, A.; Santi, I.; Mandalakis, M.; Pavlidou, A.; Lika, K.; Psarra, S. Pigmented and Heterotrophic Nanoflagellates: Abundance and Grazing on Prokaryotic Picoplankton in the Ultra-Oligotrophic Eastern Mediterranean Sea. *Deep Sea Res. Part II Top. Stud. Oceanogr.* 2019, 164, 100–111. [CrossRef]
- 97. Lagaria, A.; Mandalakis, M.; Mara, P.; Frangoulis, C.; Karatsolis, B.T.; Pitta, P.; Triantaphyllou, M.; Tsiola, A.; Psarra, S. Phytoplankton Variability and Community Structure in Relation to Hydrographic Features in the NE Aegean Frontal Area (NE Mediterranean Sea). *Cont. Shelf Res.* **2017**, *149*, 124–137. [CrossRef]
- 98. Petihakis, G.; Perivoliotis, L.; Korres, G.; Ballas, D.; Frangoulis, C.; Pagonis, P.; Ntoumas, M.; Pettas, M.; Chalkiopoulos, A.; Sotiropoulou, M.; et al. An Integrated Open-Coastal Biogeochemistry, Ecosystem and Biodiversity Observatory of the Eastern Mediterranean—The Cretan Sea Component of the POSEIDON System. *Ocean Sci.* 2018, 14, 1223–1245. [CrossRef]
- 99. Ntoumas, M.; Perivoliotis, L.; Petihakis, G.; Korres, G.; Frangoulis, C.; Ballas, D.; Pagonis, P.; Sotiropoulou, M.; Pettas, M.; Bourma, E.; et al. The POSEIDON Ocean Observing System: Technological Development and Challenges. *J. Mar. Sci. Eng.* **2022**, *10*, 1932. [CrossRef]

Remote Sens. 2025, 17, 2362 29 of 31

100. Kournopoulou, A.; Kikaki, K.; Varkitzi, I.; Psarra, S.; Assimakopoulou, G.; Karantzalos, K.; Raitsos, D.E. Atlas of Phytoplankton Phenology Indices in Selected Eastern Mediterranean Marine Ecosystems. *Sci. Rep.* **2024**, *14*, 9975. [CrossRef]

- 101. Aiken, J.; Pradhan, Y.; Barlow, R.; Lavender, S.; Poulton, A.; Holligan, P.; Hardman-Mountford, N. Phytoplankton Pigments and Functional Types in the Atlantic Ocean: A Decadal Assessment, 1995–2005. *Deep Sea Res. Part II Topical Stud. Oceanogr.* 2009, 56, 899–917. [CrossRef]
- 102. Psarra, S.; Livanou, E.; Varkitzi, I.; Lagaria, A.; Assimakopoulou, G.; Pagou, K.; Ignatiades, L. Phytoplankton Dynamics in the Aegean Sea. *Handb. Environ. Chem.* **2022**, *129*, 89–114. [CrossRef]
- 103. García, C.; Pruzzo, M.; Rodríguez-Unda, N.; Contreras, C.; Lagos, N. Zur Vervollkommung Der Quantitativen Phytoplankton-Methodik. *Mitt Int. Ver Limnol.* **1958**, *9*, 38. [CrossRef]
- 104. Psarra, S.; Tselepides, A.; Ignatiades, L. Primary Productivity in the Oligotrophic Cretan Sea (NE Mediterranean): Seasonal and Interannual Variability. *Prog. Oceanogr.* **2000**, *46*, 187–204. [CrossRef]
- 105. Galgani, L.; Tsapakis, M.; Pitta, P.; Tsiola, A.; Tzempelikou, E.; Kalantzi, I.; Esposito, C.; Loiselle, A.; Tsotskou, A.; Zivanovic, S.; et al. Microplastics Increase the Marine Production of Particulate Forms of Organic Matter. *Environ. Res. Lett.* **2019**, *14*, 124085. [CrossRef]
- 106. Oikonomou, A.; Livanou, E.; Mandalakis, M.; Lagaria, A.; Psarra, S. Grazing Effect of Flagellates on Bacteria in Response to Phosphate Addition in the Oligotrophic Cretan Sea, NE Mediterranean. *FEMS Microbiol. Ecol.* **2020**, *96*, 86. [CrossRef]
- 107. Ktistaki, G.; Magiopoulos, I.; Corno, G.; Courboulès, J.; Eckert, E.M.; González, J.; Kalantzi, I.; Middelboe, M.; Symiakaki, K.; Tsapakis, M.; et al. Brownification in the Eastern Mediterranean Sea: Effect of Simulated Terrestrial Input on the Planktonic Microbial Food Web in an Oligotrophic Sea. *Front. Mar. Sci.* 2024, 11, 1343415. [CrossRef]
- 108. Berthon, J.-F.; Zibordi, G.; Ois Berthon, J.-F.; Zibordi, G. Bio-Optical Relationships for the Northern Adriatic Sea. *Int. J. Remote Sens.* **2004**, *25*, 1527–1532. [CrossRef]
- 109. Volpe, G.; Colella, S.; Brando, V.E.; Forneris, V.; La Padula, F.; Di Cicco, A.; Sammartino, M.; Bracaglia, M.; Artuso, F.; Santoleri, R. Mediterranean Ocean Colour Level 3 Operational Multi-Sensor Processing. *Ocean Sci.* **2019**, *15*, 127–146. [CrossRef]
- 110. Concha, J.A.; Bracaglia, M.; Brando, V.E. Assessing the Influence of Different Validation Protocols on Ocean Colour Match-up Analyses. *Remote Sens. Environ.* **2021**, 259, 112415. [CrossRef]
- 111. Sathyendranath, S.; Brewin, R.J.W.; Brockmann, C.; Brotas, V.; Calton, B.; Chuprin, A.; Cipollini, P.; Couto, A.B.; Dingle, J.; Doerffer, R. An Ocean-Colour Time Series for Use in Climate Studies: The Experience of the Ocean-Colour Climate Change Initiative (OC-CCI). Sensors 2019, 19, 4285.
- 112. Pisano, A.; Buongiorno Nardelli, B.; Tronconi, C.; Santoleri, R. The New Mediterranean Optimally Interpolated Pathfinder AVHRR SST Dataset (1982–2012). *Remote Sens. Environ.* **2016**, 176, 107–116. [CrossRef]
- 113. Claustre, H. The Trophic Status of Various Oceanic Provinces as Revealed by Phytoplankton Pigment Signatures. *Limnol. Oceanogr.* **1994**, *39*, 1206–1210.
- 114. Uitz, J.; Claustre, H.; Morel, A.; Hooker, S.B. Vertical Distribution of Phytoplankton Communities in Open Ocean: An Assessment Based on Surface Chlorophyll. *J. Geophys. Res. Oceans* **2006**, *111*, C08005. [CrossRef]
- 115. Devred, E.; Sathyendranath, S.; Stuart, V.; Platt, T. Remote Sensing of Environment A Three Component Classification of Phytoplankton Absorption Spectra: Application to Ocean-Color Data. *Remote Sens. Environ.* **2011**, *115*, 2255–2266. [CrossRef]
- 116. Sathyendranath, S.; Cota, G.; Stuart, V.; Maass, H.; Platt, T. Remote Sensing of Phytoplankton Pigments: A Comparison of Empirical and Theoretical Approaches. *Int. J. Remote Sens.* **2001**, 22, 249–273. [CrossRef]
- 117. Raimbault, P. Size Fractionation of Phytoplankton in the Ligurian Sea and the Algerian Basin (Mediterranean Sea): Size Distribution versus Total Concentration. *Mar. Microb. Food Webs* **1988**, *3*, 1–7.
- 118. Efron, B. Bootstrap Methods: Another Look at the Jackknife. In *Breakthroughs in Statistics*; Springer: New York, NY, USA, 1992; pp. 569–593.
- 119. Brewin, R.J.; Hirata, T.; Hardman-Mountford, N.J.; Lavender, S.J.; Sathyendranath, S.; Barlow, R. The influence of the Indian Ocean Dipole on interannual variations in phytoplankton size structure as revealed by Earth Observation. *Deep Sea Res. Part II Top. Stud. Oceanogr.* 2012, 77, 117–127. [CrossRef]
- 120. Seegers, B.N.; Stumpf, R.P.; Schaeffer, B.A.; Loftin, K.A.; Werdell, P.J. Performance Metrics for the Assessment of Satellite Data Products: An Ocean Color Case Study. *Opt. Express* **2018**, *26*, 7404–7422. [CrossRef]
- 121. Stramski, D.; Joshi, I.; Reynolds, R.A. Ocean Color Algorithms to Estimate the Concentration of Particulate Organic Carbon in Surface Waters of the Global Ocean in Support of a Long-Term Data Record from Multiple Satellite Missions. *Remote Sens. Environ.* 2022, 269, 112776. [CrossRef]
- 122. Kong, C.E.; Sathyendranath, S.; Jackson, T.; Stramski, D.; Brewin, R.J.W.; Kulk, G.; Jönsson, B.F.; Loisel, H.; Galí, M.; Le, C. Comparison of Ocean-Colour Algorithms for Particulate Organic Carbon in Global Ocean. *Front. Mar. Sci.* **2024**, *11*, 1309050. [CrossRef]
- 123. Broomell, S.B.; Budescu, D.V.; Por, H.H. Pair-Wise Comparisons of Multiple Models. *Judgm. Decis. Mak.* **2011**, *6*, 821–831. [CrossRef]

Remote Sens. 2025, 17, 2362 30 of 31

124. Ward, B.A. Temperature-Correlated Changes in Phytoplankton Community Structure Are Restricted to Polar Waters. *PLoS ONE* **2015**, *10*, e0135581. [CrossRef]

- 125. Marty, J.C.; Chiavérini, J.; Pizay, M.D.; Avril, B. Seasonal and Interannual Dynamics of Nutrients and Phytoplankton Pigments in the Western Mediterranean Sea at the DYFAMED Time-Series Station (1991–1999). *Deep Sea Res. Part II Topical Stud. Oceanogr.* **2002**, 49, 1965–1985. [CrossRef]
- 126. Arin, L.; Morán, X.A.G.; Estrada, M. Phytoplankton Size Distribution and Growth Rates in the Alboran Sea (SW Mediterranean): Short Term Variability Related to Mesoscale Hydrodynamics. *J. Plankton Res.* **2002**, 24, 1019–1033. [CrossRef]
- 127. Ignatiades, L.; Psarra, S.; Zervakis, V.; Pagou, K.; Souvermezoglou, E.; Assimakopoulou, G.; Gotsis-Skretas, O. Phytoplankton Size-Based Dynamics in the Aegean Sea (Eastern Mediterranean). *J. Mar. Syst.* **2002**, *36*, 11–28. [CrossRef]
- 128. Psarra, S.; Zohary, T.; Krom, M.D.; Mantoura, R.F.C.; Polychronaki, T.; Stambler, N.; Tanaka, T.; Tselepides, A.; Thingstad, F. Phytoplankton Response to a Lagrangian Phosphate Addition in the Levantine Sea (Eastern Mediterranean). *Deep Sea Res. Part II Top. Stud. Oceanogr.* 2005, 52, 2944–2960. [CrossRef]
- 129. Uitz, J.; Stramski, D.; Gentili, B.; D'Ortenzio, F.; Claustre, H. Estimates of Phytoplankton Class-Specific and Total Primary Production in the Mediterranean Sea from Satellite Ocean Color Observations. *Global Biogeochem. Cycles* **2012**, *26*. [CrossRef]
- 130. Varkitzi, I.; Psarra, S.; Assimakopoulou, G.; Pavlidou, A.; Krasakopoulou, E.; Velaoras, D.; Papathanassiou, E.; Pagou, K. Phytoplankton Dynamics and Bloom Formation in the Oligotrophic Eastern Mediterranean: Field Studies in the Aegean, Levantine and Ionian Seas. *Deep Sea Res. Part II Top. Stud. Oceanogr.* 2020, 171, 104662. [CrossRef]
- 131. Jacquet, S.; Lennon, J.F.; Marie, D.; Vaulot, D. Picoplankton Population Dynamics in Coastal Waters of the Northwestern Mediterranean Sea. *Limnol. Oceanogr.* **1998**, *43*, 1916–1931. [CrossRef]
- 132. Agawin, N.S.R.; Duarte, C.M.; Agustí, S. Nutrient and Temperature Control of the Contribution of Picoplankton to Phytoplankton Biomass and Production. *Limnol. Oceanogr.* **2000**, *45*, 591–600. [CrossRef]
- 133. Cerino, F.; Bernardi Aubry, F.; Coppola, J.; La Ferla, R.; Maimone, G.; Socal, G.; Totti, C. Spatial and Temporal Variability of Pico-, Nano- and Microphytoplankton in the Offshore Waters of the Southern Adriatic Sea (Mediterranean Sea). *Cont. Shelf Res.* **2012**, 44, 94–105. [CrossRef]
- 134. van de Poll, W.H.; Boute, P.G.; Rozema, P.D.; Buma, A.G.J.; Kulk, G.; Rijkenberg, M.J.A. Sea Surface Temperature Control of Taxon Specific Phytoplankton Production along an Oligotrophic Gradient in the Mediterranean Sea. *Mar. Chem.* **2015**, 177, 536–544. [CrossRef]
- 135. Pulina, S.; Brutemark, A.; Suikkanen, S.; Padedda, B.M.; Grubisic, L.M.; Satta, C.T.; Caddeo, T.; Farina, P.; Sechi, N.; Lugliè, A. Effects of Warming on a Mediterranean Phytoplankton Community. *Web Ecol.* **2016**, *16*, 89–92. [CrossRef]
- 136. Raven, J.A. The Twelfth Tansley Lecture. Small Is Beautiful: The Picophytoplankton. New Phytol. 1998, 140, 9–13.
- 137. Morán, X.A.G.; López-Urrutia, Á.; Calvo-Díaz, A.; LI, W.K.W. Increasing Importance of Small Phytoplankton in a Warmer Ocean. *Glob. Change Biol.* **2010**, *16*, 1137–1144. [CrossRef]
- 138. Marañón, E.; Cermeño, P.; Latasa, M.; Tadonléké, R.D. Temperature, Resources, and Phytoplankton Size Structure in the Ocean. *Limnol. Oceanogr.* **2012**, *57*, 1266–1278. [CrossRef]
- 139. Ramírez-Romero, E.; Molinero, J.C.; Sommer, U.; Salhi, N.; Kéfi-Daly Yahia, O.; Daly Yahia, M.N. Phytoplankton Size Changes and Diversity Loss in the Southwestern Mediterranean Sea in Relation to Long-Term Hydrographic Variability. *Estuar. Coast. Shelf Sci.* 2020, 235, 106574. [CrossRef]
- 140. Hillebrand, H.; Acevedo-Trejos, E.; Moorthi, S.D.; Ryabov, A.; Striebel, M.; Thomas, P.K.; Schneider, M.L. Cell Size as Driver and Sentinel of Phytoplankton Community Structure and Functioning. *Funct. Ecol.* **2022**, *36*, 276–293. [CrossRef]
- 141. Marañón, E.; Holligan, P.; Barciela, R.; González, N.; Mouriño, B.; Pazó, M.; Varela, M. Patterns of Phytoplankton Size Structure and Productivity in Contrasting Open-Ocean Environments. *Mar. Ecol. Prog. Ser.* **2001**, 216, 43–56. [CrossRef]
- 142. Leblanc, K.; Quéguiner, B.; Diaz, F.; Cornet, V.; Michel-Rodriguez, M.; Durrieu De Madron, X.; Bowler, C.; Malviya, S.; Thyssen, M.; Grégori, G.; et al. Nanoplanktonic Diatoms Are Globally Overlooked but Play a Role in Spring Blooms and Carbon Export. *Nat. Commun.* 2018, 9, 953. [CrossRef]
- 143. Marty, J.C.; Chiavérini, J. Hydrological Changes in the Ligurian Sea (NW Mediterranean, DYFAMED Site) during 1995-2007 and Biogeochemical Consequences. *Biogeosciences* **2010**, *7*, 2117–2128. [CrossRef]
- 144. Ciavatta, S.; Kay, S.; Brewin, R.J.W.; Cox, R.; Di Cicco, A.; Nencioli, F.; Polimene, L.; Sammartino, M.; Santoleri, R.; Skákala, J.; et al. Ecoregions in the Mediterranean Sea Through the Reanalysis of Phytoplankton Functional Types and Carbon Fluxes. *J. Geophys. Res. Oceans* **2019**, 124, 6737–6759. [CrossRef]
- 145. Pan, X.; Wong, G.T.F.; Ho, T.Y.; Shiah, F.K.; Liu, H. Remote Sensing of Picophytoplankton Distribution in the Northern South China Sea. *Remote Sens. Environ.* **2013**, *128*, 162–175. [CrossRef]
- 146. Mozetič, P.; Francé, J.; Kogovšek, T.Š.; Talaber, I.; Malej, A. Plankton Trends and Community Changes in a Coastal Sea (Northern Adriatic): Bottom-up vs. Top-down Control in Relation to Environmental Drivers. *Estuar. Coast. Shelf Sci.* 2012, 115, 138–148. [CrossRef]

Remote Sens. 2025, 17, 2362 31 of 31

147. Maugendre, L.; Gattuso, J.P.; Louis, J.; De Kluijver, A.; Marro, S.; Soetaert, K.; Gazeau, F. Effect of Ocean Warming and Acidification on a Plankton Community in the NW Mediterranean Sea. *ICES J. Mar. Sci.* **2015**, *72*, 1744–1755. [CrossRef]

- 148. Li, M.; Organelli, E.; Serva, F.; Bellacicco, M.; Landolfi, A.; Pisano, A.; Marullo, S.; Shen, F.; Mignot, A.; van Gennip, S.; et al. Phytoplankton spring bloom inhibited by marine heatwaves in the North-Western Mediterranean Sea. *Geophys. Res. Lett.* **2024**, 51, e2024GL109141. [CrossRef]
- 149. Neri, F.; Garzia, A.; Ubaldi, M.; Romagnoli, T.; Accoroni, S.; Coluccelli, A.; Di Cicco, A.; Memmola, F.; Falco, P.; Totti, C. Ocean Warming, Marine Heatwaves and Phytoplankton Biomass: Long-Term Trends in the Northern Adriatic Sea. *Estuar. Coast. Shelf Sci.* 2025, 322, 109282. [CrossRef]
- 150. Behrenfeld, M.J.; O'Malley, R.T.; Siegel, D.A.; McClain, C.R.; Sarmiento, J.L.; Feldman, G.C.; Milligan, A.J.; Falkowski, P.G.; Letelier, R.M.; Boss, E.S. Climate-Driven Trends in Contemporary Ocean Productivity. *Nature* **2006**, 444, 752–755. [CrossRef]
- 151. Bopp, L.; Aumont, O.; Cadule, P.; Alvain, S.; Gehlen, M. Response of Diatoms Distribution to Global Warming and Potential Implications: A Global Model Study. *Geophys. Res. Lett.* **2005**, *32*, L19606. [CrossRef]
- 152. Hirata, T.; Aiken, J.; Hardman-Mountford, N.; Smyth, T.J.; Barlow, R.G. An Absorption Model to Determine Phytoplankton Size Classes from Satellite Ocean Colour. *Remote Sens. Environ.* **2008**, *112*, 3153–3159. [CrossRef]
- 153. Brewin, R.J.W.; Sathyendranath, S.; Lange, P.K.; Tilstone, G. Comparison of Two Methods to Derive the Size-Structure of Natural Populations of Phytoplankton. *Deep Sea Res. I Oceanogr. Res. Pap.* **2014**, *85*, 72–79. [CrossRef]
- 154. Worden, A.Z.; Nolan, J.K.; Palenik, B. Assessing the Dynamics and Ecology of Marine Picophytoplankton: The Importance of the Eukaryotic Component. *Limnol. Oceanogr.* **2004**, *49*, 168–179. [CrossRef]
- 155. Shi, X.L.; Lepère, C.; Scanlan, D.J.; Vaulot, D. Plastid 16S RRNA Gene Diversity among Eukaryotic Picophytoplankton Sorted by Flow Cytometry from the South Pacific Ocean. *PLoS ONE* **2011**, *6*, e18979. [CrossRef]
- 156. Rii, Y.M.; Duhamel, S.; Bidigare, R.R.; Karl, D.M.; Repeta, D.J.; Church, M.J. Diversity and Productivity of Photosynthetic Picoeukaryotes in Biogeochemically Distinct Regions of the South East Pacific Ocean. *Limnol. Oceanogr.* **2016**, *61*, 806–824. [CrossRef]
- 157. Shi, X.L.; Marie, D.; Jardillier, L.; Scanlan, D.J.; Vaulot, D. Groups without Cultured Representatives Dominate Eukaryotic Picophytoplankton in the Oligotrophic South East Pacific Ocean. *PLoS ONE* **2009**, *4*, e7657. [CrossRef]
- 158. Lagaria, A.; Mandalakis, M.; Mara, P.; Papageorgiou, N.; Pitta, P.; Tsiola, A.; Kagiorgi, M.; Psarra, S. Phytoplankton Response to Saharan Dust Depositions in the Eastern Mediterranean Sea: A Mesocosm Study. *Front. Mar. Sci.* **2017**, *3*, 230802. [CrossRef]
- 159. Man-Aharonovich, D.; Philosof, A.; Kirkup, B.C.; Le Gall, F.; Yogev, T.; Berman-Frank, I.; Polz, M.F.; Vaulot, D.; Béjà, O. Diversity of Active Marine Picoeukaryotes in the Eastern Mediterranean Sea Unveiled Using Photosystem-II PsbA Transcripts. *ISME J.* **2010**, *4*, 1044–1052. [CrossRef] [PubMed]
- 160. Wu, W.; Guo, C.; Pitta, P.; Liu, H. Response of Active Picoeukaryotes to the Deposition of Saharan Dust and European Aerosols in the Eastern Mediterranean Sea. *Aquat. Microb. Ecol.* **2018**, *82*, 31–42. [CrossRef]
- 161. Chase, A.P.; Kramer, S.J.; Haëntjens, N.; Boss, E.S.; Karp-Boss, L.; Edmondson, M.; Graff, J.R. Evaluation of Diagnostic Pigments to Estimate Phytoplankton Size Classes. *Limnol. Oceanogr. Methods* **2020**, *18*, 570–584. [CrossRef]
- 162. Hirata, T.; Hardman-Mountford, N.J.; Brewin, R.J.W.; Aiken, J.; Barlow, R.; Suzuki, K.; Isada, T.; Howell, E.; Hashioka, T.; Noguchi-Aita, M.; et al. Synoptic Relationships between Surface Chlorophyll-a and Diagnostic Pigments Specific to Phytoplankton Functional Types. *Biogeosciences* 2011, *8*, 311–327. [CrossRef]
- 163. Specchia, V.; Zangaro, F.; Tzafesta, E.; Saccomanno, B.; Vadrucci, M.R.; Pinna, M. Environmental DNA Detects Biodiversity and Ecological Features of Phytoplankton Communities in Mediterranean Transitional Waters. *Sci. Rep.* **2023**, *13*, 15192. [CrossRef]

Disclaimer/Publisher's Note: The statements, opinions and data contained in all publications are solely those of the individual author(s) and contributor(s) and not of MDPI and/or the editor(s). MDPI and/or the editor(s) disclaim responsibility for any injury to people or property resulting from any ideas, methods, instructions or products referred to in the content.